A STUDY OF IMMERSED BOUNDARY METHOD IN A RIBBED DUCT FOR THE INTERNAL COOLING OF TURBINE BLADES

Long He

Thesis submitted to the faculty of the Virginia Polytechnic Institute and State University in partial fulfillment of the requirements for the degree of

Master of Science
in
Mechanical Engineering

Danesh K. Tafti – Chair
Clinton L. Dancey
Srinath Ekkad

December 8, 2014
Blacksburg, Virginia, USA

Keywords: immersed boundary method, turbine heat transfer, internal cooling, wall model

A STUDY OF IMMERSED BOUNDARY METHOD IN A RIBBED DUCT FOR THE INTERNAL COOLING OF TURBINE BLADES

Long He

Abstract

In this dissertation, Immersed Boundary Method (IBM) is evaluated in ribbed duct geometries to show the potential of simulating complex geometry with a simple structured grid. IBM is first investigated in well-accepted benchmark cases: channel flow and pipe flow with circular cross-section. IBM captures all the flow features with very good accuracy in these two cases. Then a two side ribbed duct geometry is test using IBM at Reynolds number of 20,000 under fully developed assumption. The IBM results agrees well with body conforming grid predictions. A one side ribbed duct geometry is also tested at a bulk Reynolds number of 1.5×10^4. Three cases have been examined for this geometry: a stationary case; a case of positive rotation at a rotation number ($Ro = \Omega D_h/U$) of 0.3 (destabilizing); and a case of negative rotation at $Ro = -0.3$ (stabilizing). Time averaged mean, turbulent quantities are presented, together with heat transfer. The overall good agreement between IBM, BCG and experimental results suggests that IBM is a promising method to apply to complex blade geometries. Due to the disadvantage of IBM that it requires large amount of cells to resolve the boundary near the immersed surface, wall modeled LES (WMLES) is evaluated in the final part of this thesis. WMLES is used for simulating turbulent flow in a developing staggered ribbed U-bend duct. Three cases have been tested at a bulk Reynolds number of 10^5: a stationary case; a positive rotation case at a rotation number $Ro = 0.2$; and a negative rotation case at $Ro = -0.2$. Coriolis force effects are included in the calculation to evaluate the wall model under the influence of these effects which are known to affect shear layer turbulence production on the leading and trailing sides of the duct. Wall model LES prediction shows good agreement with experimental data.

Dedicated to Mom and Dad

It's impossible to thank you adequately for everything you've done.

Acknowledgements

First and foremost, I would like to use this opportunity to express my gratitude to Dr. Danesh Tafti for his excellent guidance, patience, and providing me with an excellent atmosphere for doing research. In the past two years, he has provided insightful discussions about my research and been a great source of knowledge to me. Without his guidance and persistent help, this dissertation would not have been possible.

I also thank Dr. Clinton Dancey and Dr. Srinath Ekkad for taking time off their busy schedules to be on my committee and reviewing my work.

I will forever be thankful to my colleagues in the lab through the past two years—Nagendra, Amit, Surya, Sukhjinder, Vivek, Handan, Husam, Deepu, Ravishankar and Keyur, who have shared their knowledge and brilliant ideas with me. I would like to extend a special thanks to Nagendra, Amit and Vivek for teaching me aspects of immersed boundary method, UNIX, Pointwise and helping with a lot of the simulation setup ideas.

I also thank the support provided by Advanced Research Computing at Virginia Tech.

Table of Contents

List of Figures

List of Tables

Chapter 1

Introduction

1.1 Motivation

Gas turbines are widely used for aircraft propulsion and land based power generation. Aiming to achieve higher thermal efficiency and power output, turbine blades operate at high inlet temperatures ($2500 - 2600F$). This operating temperature is far above the permissible blade metal temperature[1]. The blade durability is highly affected by the temperature level and variation within the blade material. Therefore, active cooling technologies are used to cool the high pressure stage nozzle vanes and blades to keep the metal temperature much below the melting point[2]. In response to this need, the modern high-pressure gas turbine blade is not only designed for aerodynamics and structural strength but also for effective cooling. This is achieved by bleeding air at a relatively cooler temperature (about 600-700 C) from compressor bypass and circulating it through internal passages in the blade or through the skin (internal cooling) and ejected into the hot gas mainstream to protect the blade surface from the hot mainstream gases (film cooling)[3]. This bleed air always comes with a performance loss and, thus, an accurate prediction of heat transfer in the cooling passage is needed to minimize this loss while keeping the turbine blades at acceptable operating temperatures.

Figure 1.1 shows a typical high pressure turbine blade model consisting of internal passages fed by cooling air at the base through the rotor hub. It has four cooling passages, one cooling the leading edge, another cooling the trailing edge, with a two pass passage at the center of the blade. In practice, a variety of heat transfer augmentation techniques are utilized in the internal passages in the form of flow turbulators (ribs, pins, dimples, protrusions), and impingement cooling to promote

turbulence and enhance heat transfer coefficients. In the example blade shown, the internal passage are equipped with ribs and the cool air is ejected out on to the blade surface on the pressure side at the leading edge, at the trailing edge, and at the blade tip.

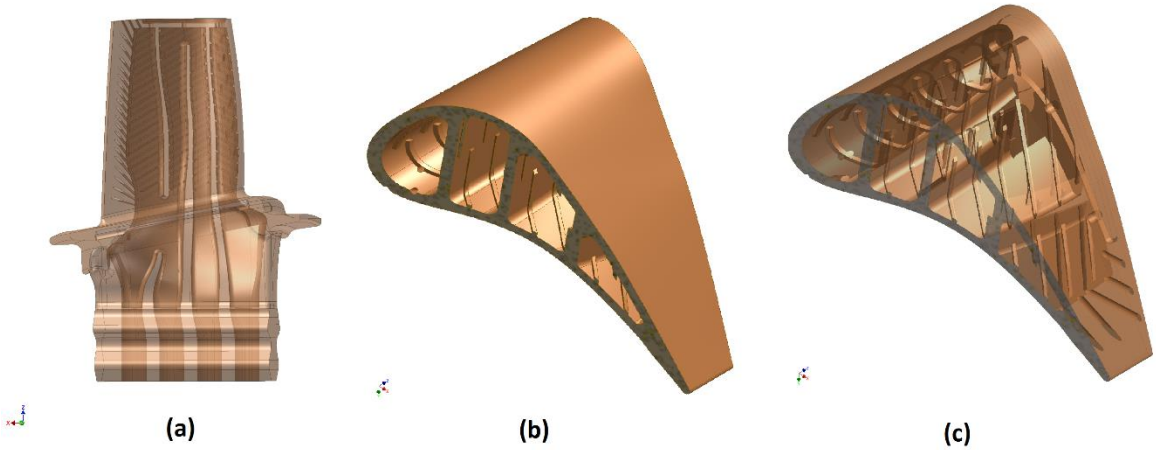

Figure 1.1: Typical high-pressure turbine blade (courtesy: Rolls-Royce). CAD geometry of blade (a-c)

A big challenge to get an accurate heat transfer prediction for the cooling passage in the blade shown above is to create a good quality structure mesh. The passage follows the curve shape of the blade, and the cross section of the passage is changing along the radius direction which makes the outer boundary of the body conforming mesh hard to generate. Along the inner surface of the passage, rib turbulators are employed following a staggered arrangement. The ribs only cover half of the passage, and the side surface of the rib have a 60 degree angle to the passage surface, shown in Figure 1.1(c). These ribs require the structured mesh to be broken into several blocks and each block needs to be carefully examined to not only match the geometrical features but also have good resolution near the surface to properly resolve the boundary layer. These intricate geometrical

features make creating a good quality grid for stable time-integration and suitable resolution of turbulence very time consuming.

In this thesis, a frame work based on Immersed Boundary Method (IBM) is used to resolve the intricate geometrical features in the simulation model. In this frame work, complex geometry surface is immersed into a volume background grid. The immersed surface cuts through the background mesh and applies proper boundary conditions for the fluid domain. In this frame work, the unstructured surface mesh can be easily generated in meshing software like Pointwise; the background mesh, because it doesn't need to resolve the intricate geometrical feature, can also be generated without expending too much effort. However, there are also some disadvantages of this method. Since the surface is not resolved exactly as in a body conforming grid, very fine mesh is required in the vicinity of the immersed boundary to get good resolution. The fineness of the grid is directly related to the Reynolds number of the flow, and the total number of computational cells for the simulation increases in proportion to the number of cells needed in the near wall region. For this reason, IBM has mostly been applied to low Reynolds number flows. To ease this grid requirement, Wall Modeled LES (WMLES) is also introduced in this thesis. In wall modeled LES, the first layer of cells can be located at about $y^+ = 20 - 50$ instead of $y^+ = 1$ from the wall. This allows the near wall grid size to be much coarser, and reduce the total computational cells required.

This thesis is organized as follows:

- In Chapter 2, governing equations and relevant terms for fully developed flow calculations are presented. The frame work of immersed boundary method and wall model LES is briefly described to give an overview of how the calculations were carried out.

- In Chapter 3, IBM is tested for two benchmark turbulent flow simulations: fully developed turbulent channel flow at $Re_\tau = 180$ and fully developed pipe flow at $Re_\tau = 338$. IBM simulation data are compared with well recognized DNS results and experiments.

- In Chapter 4, IBM is used for rib duct simulation. Two rib duct geometries are tested. In case 1, simulation is performed for a stationary fully developed rib duct at Re = 20,000. Results are compared with former body conformed grid results (Tafti,2006). In case two, a one side ribbed duct is simulated at stationary, negative and positive rotation condition at Re = 15,000. Simulation results are compared with PIV experiment data.

- In Chapter 5, wall modeled LES simulation is performed for a developed U-bend rib duct at Re = 100,000, stationary, a rotation number Ro = 0.3 and a rotation number Ro = -0.3. Flow behavior is observed against experimental data.

- This thesis is summarized in Chapter 6 with concluding remarks.

1.2 Literature review

A significant number of experimental and numerical investigations of flow field and heat transfer in the ribbed duct have been conduct since the 1970s. In the earliest studies, many fundamental studies have been conducted in stationary ribbed ducts.

Han and research group at Texas A&M [4][5][6][7][8][9][10] have studied the effect of different rib orientations, different rib angles, different rib height/hydraulic diameter ratios, different rib pitch/height ratios, different aspect ratio channels in a Reynolds number range from 10,000 to 100,000. According to these studies, the geometry and arrangement of the rib turbulator have significant effects on the local mass and heat transfer distributions.

In a rotating cooling passage, the effects of Coriolis and buoyancy forces alter the flow and temperature profiles and affect the heat transfer coefficient distributions on the surfaces [11]. Many experiments have been conducted focusing on the effects of rotation.

Liou [12] conducted an LDV experiment study of the flow field in a 180 degree straight-corner. The experiment was performed with the rotation number of 0 and 0.082. The data showed that rotating the duct augmented and shifted the peaks of the streamwise mean velocity and turbulence intensity profiles toward the trailing and leading walls of the first and second passes, respectively. They[13] also studied heat transfer and fluid flow in a rotating two-pass duct with 90 °ribs at Reynolds number of 10,000 by using Laser Doppler Velocimetry (LDV) and transient thermochromic liquid crystal measurements. The rib to pitch e/P was 0.1 and rib to hydraulic diameter e/D_h was 0.136, respectively. The rotation number was varied from 0 to 0.2. The experiment data showed that on the trailing side of the first pass, heat transfer was systematically increased with an increase of rotation number, while on the leading side of the first pass, heat transfer was reduced.

In another study by Taslim et al. [14], the Reynolds number was varied from 15,000 to 50,000, the e/D_h was varied between 0.133, 0.25 and 0.333. The rotation number was varied from 0.01 to 0.1 in the experiment. The results showed that heat transfer increased by a maximum of 45% for e/D_h of 0.133 and decreased by 6% for e/D_h of 0.333 compared to the stationary case.

Wagner et al.[15] studied 90 °rounded ribs in a rotating duct at Reynolds number of 25,000. The density ratio was varied from 0 to 0.23 and rotation number ranged from 0 to 0.23. The experimental results showed that rotation contributed significantly to the overall heat transfer for radially inward and radially outward flow.

A developing orthogonal rotating ribbed duct at bulk Reynolds number of 15,000 was studied by Coletti [16] using two-dimensional particle image velocimetry (PIV). The rotation number was varied from 0.3 to 0.38. They presented the detailed velocity field and turbulent statistics in the central plane. They observed that, compared to the stationary case, the reattachment point moved downstream (upstream) for stabilizing (destabilizing) rotation. Coriolis forces indirectly affected the production of turbulent kinetic energy via the Reynolds shear stress and the mean shear.

A vast number of numerical simulations have been performed to investigate the ability of the turbulence models to predict the flow field and heat transfer in cooling duct. Early research has mostly been conducted with the use of the Reynolds-Averaged Navier-Stokes (RANS) with a variety of turbulence models ranging from two-equation eddy-viscosity models such as the k-ε, k-ω SST, v2-f model [17], algebraic stress models (ASM) [18][19] to full Reynolds stress closure with varying degrees of success [3].

Iacovides and Launder[20] simulated fully developed flow in a rotating rectangular duct. The bulk of the flow was calculated based on the standard high Reynolds number k-ε model; in the near wall region, a low Reynolds number one-equation model was used. The predictions captured the secondary flow correctly and showed qualitative agreement with the experimental heat transfer data.

Bo et al.[21] studied developing flow in an orthogonally rotating square duct under two rotation numbers. The simulations were performed with three turbulence models: a low Reynolds number k-ε eddy viscosity model (EVM), a low Reynolds number algebraic stress model, and an EVM with a low Reynolds number one-equation EVM near the wall. The first model gave the best result when buoyancy effects were considered; the second model performed well when the rotation was low; the third model gave very poor results.

In the recent two decades, the increasing computational power and capacity has made the Large Eddy Simulations (LES) [22][23][24][25] and hybrid methods using RANS(URANS)-LES or detached eddy simulations (DES) [26][27] become possible [3].

Watanabe and Takahashi [28] performed LES simulations for fully developed non-rotating ribbed duct flow with Re=107,000 based on the bulk velocity. The duct had an aspect ratio of 0.5 and 90 °ribs with $e/D_h = 0.1$ and $P/e = 10$, respectively. The results agreed well with the experimental results presented in their paper.

Saha and Acharya [29] simulated a rib duct model with ribs in a staggered arrangement at Re=12,500 under stationary and rotating conditions (Ro=1.2). They performed LES calculation with the dynamic Smagorinsky model. Comparing to the experiments, the simulation over predicted the heat transfer augmentation values by 30% in the stationary case. In the rotating case, the prediction was within 20% of the experimental data.

Abdel-Wahab and Tafti [30]evaluated LES in rotating ducts at Reynolds number of 20,000. The rotation number was varied between 0.18, 0.35 and 0.67. Their results showed that heat transfer augmentation on the leading surface kept decreasing with an increasing in rotation number. On the smooth wall, the heat transfer coefficient increased by 20% to 30% comparing to the stationary case. Their results showed good agreement with the experimental data.

Chapter 2

Numerical Methodology

All the calculations are performed using an in-house code – Generalized Incompressible Direct and Large Eddy Simulation of Turbulence (GenIDLEST). The details of the framework and methodology used in GenIDLEST can be found in Tafti [31]also Tafti [32]. In this chapter, the relevant governing equations and the modified treatment of the governing equations under fully-developed conditions is given together with some elements of the immersed boundary method [33] and the wall model used for LES [34].

2.1 Governing Equations

The non-dimensional form of the Navier-Stokes equations for incompressible flow are as follows:

Continuity:

$$\frac{\partial \mathrm{u}_i}{\partial x_i} = 0 \qquad \textbf{Equation 2.1}$$

Momentum:

$$\frac{\partial u_i}{\partial \mathrm{t}} + \frac{\partial (u_j u_i)}{\partial x_j} = -\frac{\partial P}{\partial x_i} + \frac{1}{Re}\left(\frac{\partial^2 u_i}{\partial x_j \partial x_j}\right) - 2Ro\, u_m \epsilon_{i3m} \qquad \textbf{Equation 2.2}$$

Energy:

$$\frac{\partial \mathrm{T}}{\partial \mathrm{t}} + \frac{\partial (u_j T)}{\partial x_j} = \frac{1}{Re \cdot Pr}\left(\frac{\partial^2 T}{\partial x_j \partial x_j}\right) \qquad \textbf{Equation 2.3}$$

Where the non-dimensionalizations are:

$$x_i = \frac{x_i^*}{L_{ref}^*}\,;\; u_i = \frac{u_i^*}{L_{ref}^*}\,;\; t = \frac{t^* u_{ref}^*}{L_{ref}^*}\,;\; p = \frac{P^* - P_{ref}^*}{\rho_{ref}^* u_{ref}^{*2}}\,;\; T = \frac{T^* - T_{ref}^*}{T_c^*}\,;\; Re = \frac{\rho_{ref}^* u_{ref}^* L_{ref}^*}{\mu_{ref}^*}\,;\; Ro = \frac{\omega_z L_{ref}^*}{\mu_{ref}^*}$$

The above governing equations are transformed to generalized coordinates and discretized with a conservative finite-volume formulation using a second-order central (SOC) difference scheme on a non-staggered grid topology. The Cartesian velocities, pressure and temperature are calculated and stored at the cell center, whereas the fluxes are calculated and stored at cell faces. A projection method using second order predictor-corrector steps is used for the time integration of the continuity and momentum equations. In the predictor step, an intermediate velocity field is calculated; and in the corrector step, the updated divergence free velocity is calculated at the new time-step by solving a pressure-Poisson equation.

2.2 Fully developed calculations

Fully developed calculations are performed by using periodic boundary conditions in each repeating representative unit in the stream-wise direction. For the pressure field, a constant mean pressure gradient is employed to balance the form and friction losses and the total pressure is expressed in terms of the mean pressure and a fluctuating or periodic component. Similarly, for constant heat flux boundary condition, the temperature field is decomposed into a mean temperature and a fluctuating temperature. The formulation is outlined here briefly. The detailed procedure used can be found in Patankar [35] and Zhang [36].

A friction velocity $u_\tau^* = \sqrt{\tau_{w_{eq}}^*/\rho^*}$ is used as the characteristic velocity scale in the Navier-Stokes equations. By using the conservation of momentum for the control volume of the periodic domain, the reference velocity can be written as:

$$u^*_{ref} = u^*_\tau = \sqrt{\tau^*_{w_{eq}}/\rho^*} = \sqrt{(-\frac{\Delta P^*_x}{L^*_x})(\frac{D^*_H}{4\rho^*})} \qquad \textbf{Equation 2.4}$$

Where

ΔP^*_x mean pressure drop in the flow direction

L^*_x periodic domain length

D^*_H hydraulic diameter

ρ^* density

$\tau^*_{w_{eq}}$ equivalent wall shear stress which includes form losses in the domain

The temperature is non-dimensionalized with the characteristic temperature $T^*_0 = q^*_w L^*_{ref}/\kappa^*$ in which L^*_{ref} is the characteristic length scale and q^*_w is the constant heat flux applied at the wall boundaries. The assumed periodicity of the domain in the stream-wise direction requires that the mean gradients of pressure and temperature are isolated from the fluctuating periodic component as follows:

$$P^*(\vec{x}, t) = P^*_{ref} - \beta^* \cdot x^* + p^*(\vec{x}, t) \qquad \textbf{Equation 2.5}$$

$$T^*(\vec{x}, t) = T^*_{ref} + \gamma^* \cdot x^* + \theta^*(\vec{x}, t) \qquad \textbf{Equation 2.6}$$

Where

β^* mean stream-wise pressure gradient $-\Delta P^*_x/L^*_x$

p^* periodic pressure fluctuation

γ^* mean stream-wise temperature gradient

θ^* periodic temperature fluctuation

The non-dimensionalized form of the above equations can be written as :

$$P(\vec{x},t) = -\beta \cdot x + p(\vec{x},t) \qquad \textbf{Equation 2.7}$$

$$T(\vec{x},t) = \gamma \cdot x + \theta(\vec{x},t) \qquad \textbf{Equation 2.8}$$

Where

$\beta = {}^{4}/_{D_H}$ and $\gamma = \Omega_s/(Re \cdot Pr \cdot Q_x \cdot L_x)$.

Ω_s heat transfer surface area

Q_x x-directional flow rate

L_x computational domain length

With the unchanged continuity equation, the momentum and the energy equation can be write as :

Momentum conservation

$$\frac{\partial u_i}{\partial \mathrm{t}} + \frac{\partial (u_j u_i)}{\partial x_j} = -\frac{\partial p}{\partial x_i} + \frac{1}{Re}\left(\frac{\partial^2 u_i}{\partial x_j \partial x_j}\right) + \beta \vec{e}_x - 2Ro_\tau u_m \epsilon_{i3m} \qquad \textbf{Equation 2.9}$$

Energy conservation

$$\frac{\partial \theta}{\partial \mathrm{t}} + \frac{\partial (u_j \theta)}{\partial x_j} = \frac{1}{Re \cdot Pr}\left(\frac{\partial^2 \theta}{\partial x_j \partial x_j}\right) - \gamma u_x \qquad \textbf{Equation 2.10}$$

Where the $\beta \vec{e}_x$ in Equation 2.9 is the mean applied pressure gradient source term. This term will balance the form and friction losses in the flow direction. The Coriolis forces are represented by $2Ro_\tau u_m \epsilon_{i3m}$ in Equation 2.9, where $Ro_\tau = \frac{\omega D_H}{U_\tau}$. The $-\gamma u_x$ in Equation 2.10 is the heat sink term to balance the energy added by the heat flux at the walls.

2.3 Immersed boundary framework

The immersed boundary methodology (IBM) presented here is an extension of a scheme first proposed by Gilmanov and Sotiropoulos [37] to a curvilinear coordinate system on a non-staggered grid. In this method, the governing equations can be solved without modification for the nodes in the fluid domain. Special treatment is only applied to the first layer of the fluid nodes next to the immersed boundary. Hence, several different turbulence models (DNS, LES, RANS, etc.) can be used along with IBM. The details of this framework and methodology can be found in Nagendra et al [33].

As an example, a simple 2-D geometry is presented here. The geometry and boundary condition is shown in Figure 2.1. Instead of creating the boundary conformed grid, an immersed boundary method is used to simulate the circular wall in the fluid domain. The major steps of the IBM implementation are summarized here.

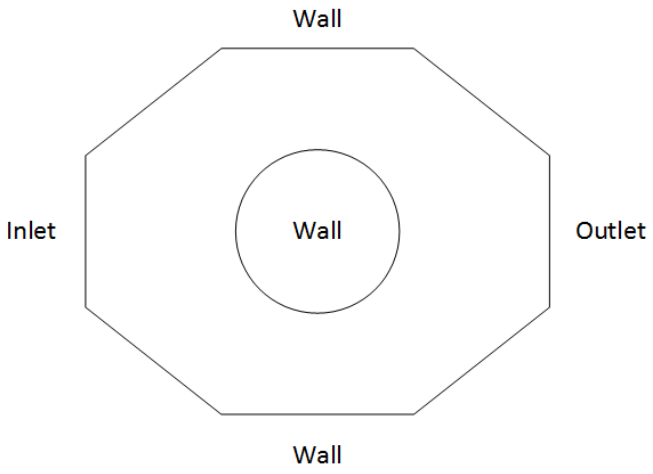

Figure 2.1: 2-D simulation geometry and boundary condition.

In the first step, the solid boundary to be modeled as immersed boundary is provided as input in a discretized form – line segment in 2D (unstructured triangular grid in 3D). Each of the segment (triangle in 3D) contains the information regarding its location with respect to the fixed background

fluid grid, normal and length (area in 3D). The surface normal is used to decide which side of the immersed boundary is solid. The grid input for the 2D problem before is shown in Figure 2.2 .Length (area in 3D) of the surface grid is used in post processing to calculate the surface forces, heat flux, etc.

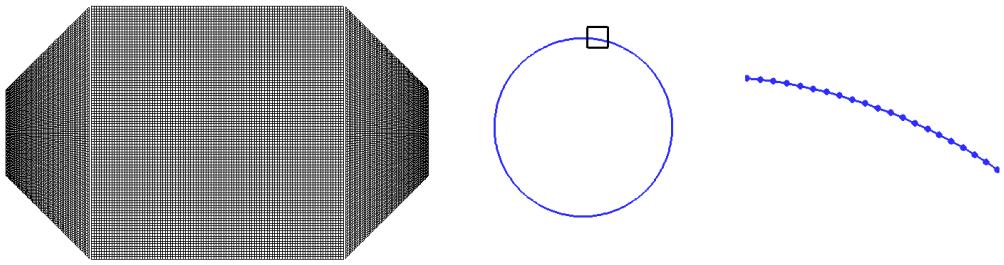

Figure 2.2: Background mesh (left) ; surface grid(middle and right).

By employing a search-locate and interpolate algorithm, the nodes in the vicinity of the immersed boundary are marked in the background mesh. Then the type (fluid or solid) of these nodes is determined based on the surface grid. These nodes will form a fluid/solid boundary on the background mesh. All the nodes inside the solid boundary will be assigned as solid node and the rest will be fluid nodes. Moreover, the fluid (solid) nodes that lie in the immediate vicinity of the immersed boundary will be assigned as fluid (solid) IB nodes. At this point, all the nodes in the background are assigned as one of the following nodetypes: fluid node, solid node, fluid ib node or solid Ib node (Solid ib node is only used for conjugate heat transfer). Figure 2.3 shows the nodetype assigned on the background mesh for the 2D simulation.

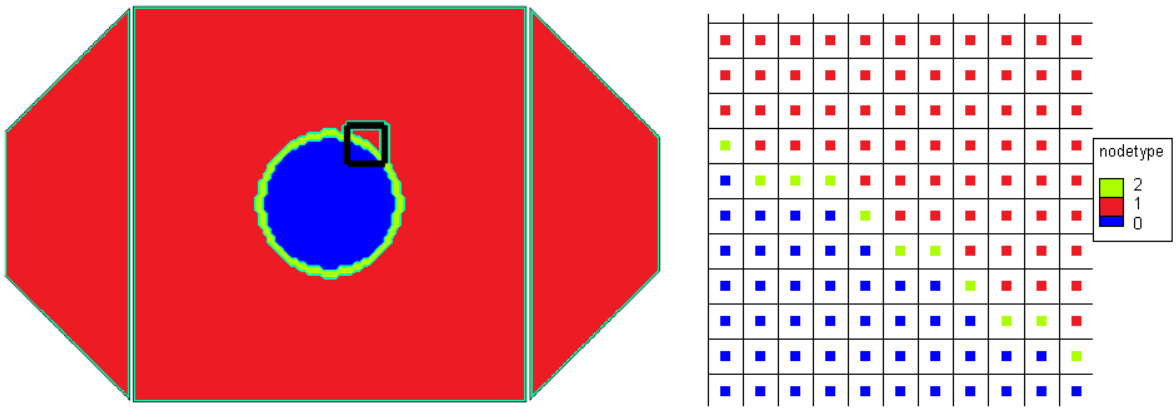

Figure 2.3: Nodetype assigned in the domain. (Nodetype: solid is 0, fluid is 1, fluid ibnode is 2)

In the second step, the governing equations will be solved for all the fluid node – all the nodes marks as 1 in Figure 2.3.

In the third step, modifications are made on the IB node values in order for the fluid and solid nodes to see the presence of the immersed boundary. For each of the IB nodes, a probe is assigned which lies on the surface grid normal direction and one cell distance from the IB node. The IB node probe location is shown in Figure 2.4. A tri-linear interpolation method is used to determine the value of the desired primitive flow variable at the probe location from the surrounding nodes. The value obtained at the probe is then utilized in the computation of the value at IB node to satisfy the appropriate boundary condition.

For Dirichlet conditions, the assumption is made that the gradient in the region between the IB surface and the probe location is constant. This leads to the following formulation:

$$\phi_{ib} = \frac{d_{ib} \cdot \phi_{p1} + (d_{p1} - d_{ib}) \cdot \phi_{BC}}{d_{p1}} \qquad \textbf{Equation 2.11}$$

For Neumann condition, for first-order accuracy, the formulation can be written as:

$$\phi_{ib} = \phi_{p1} - (d_{p1} - d_{ib}) \cdot \frac{\partial \phi}{\partial n}\Big|_{BC} \qquad \textbf{Equation 2.12}$$

When the governing equations are solved at the fluid nodes in the next time step, these IB nodes values will be used. Hence, the presence of the immersed boundary will be seen by the nodes in the fluid region.

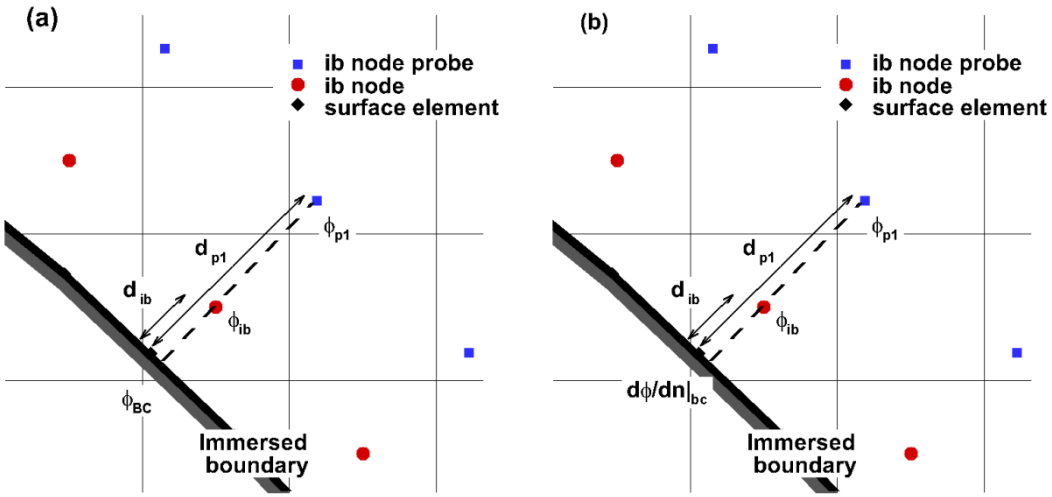

Figure 2.4: Dirichlet condition (a); Neumann condition (b).

2.4 Wall Modeled LES

Large eddy simulation has the advantage that it constitutes a good compromise between predictive accuracy and computational cost. LES directly resolves energetic, dynamically important and flow-dependent eddy motions allowing better fidelity than Reynolds-Averaged Navier–Stokes (RANS) methods. The low-pass filtering operation applied to the Navier-Stokes equations allows motions with small energy and supposedly universal behavior to be modeled which reduces the computational cost. However, when LES is applied to turbulent boundary layers, near wall resolution

requirements increase tremendously because the energetic and dynamically important motions in the inner boundary layer become progressively small as the Reynolds number increases [38]. This requirement leads to very fine grids in the inner boundary layer, increasing the computational cost. Therefore, modeling the inner layer is necessary for high Reynolds number LES [39].

The zonal model or two-layer model (TLM) is present here. More detail can be found in [34]. In this method, filtered Navier-Stokes equations are solved in the outer grid, while in the inner layer modified equations are solved on a virtual grid which is embedded between the wall and the first grid point off the wall. The coupling between the inner and outer layer is accomplished by using the instantaneous outer flow velocity as a boundary condition to the inner layer. By solving a suitable set of reduced equations with a suitable approximation for the eddy-viscosity in the inner layer, the calculated velocity profile in the inner layer is used to compute the wall shear stress. The wall shear stress is then used as a boundary condition in the calculation of the outer layer equations at the first off-wall grid.

In the inner layer, a local coordinate system (*n*, *t*) is used, where *n* is normal to the surface, and *t* is the tangential direction. An effective simplified tangent momentum transport equation is constructed for the inner layer by neglecting the advection terms and tangential diffusion as:

$$\frac{\partial}{\partial n}\left[\left(\frac{1}{Re}+\frac{1}{Re_t}\right)\frac{\partial u_t}{\partial n}\right]=\frac{\partial \mathrm{P}}{\partial \mathrm{t}} \qquad \textbf{Equation 2.13}$$

With $u_t = 0$ at the wall and $u_t = \left\|\vec{U}_t\right\|$ at the first LES grid point.

The eddy-viscosity is modeled by

$$\frac{1}{Re_t} = \frac{\kappa}{Re} d^+ (1 - e^{-d^+/A})^2$$

$$d^+ = \rho u_\tau d/\mu \qquad \textbf{Equation 2.14}$$

$$u_\tau = \sqrt{\|\tau_w\|/\rho}$$

Where κ is the Von Karman constant, d is the normal distance from the wall, and $A = 19$. The one-dimensional equation is solved by using a standard tri-diagonal solver with second-order central difference approximation.

After Equation 2.13 is solved, the magnitude of the tangential shear stress can be solved as:

$$\|\tau_w\| = \frac{1}{Re} \frac{\partial u_t}{\partial n}\Big|_{wall} \qquad \textbf{Equation 2.15}$$

The shear stress is translated back to the coordinate system used by the LES as:

$$\vec{\tau}_w = \|\tau_w\|\vec{t} = \|\tau_w\| t_x \vec{e}_x + \|\tau_w\| t_y \vec{e}_y + \|\tau_w\| t_z \vec{e}_z \qquad \textbf{Equation 2.16}$$

Where $\vec{t}$ is the unit tangential vector and

$$\frac{1}{Re} \frac{\partial u_i}{\partial n}\Big|_{wall} = \|\tau_w\| t_i \qquad \textbf{Equation 2.17}$$

These stress components at the wall now can be used as the boundary conditions for solving the discretized momentum equations at the first grid point normal to the wall.

Chapter 3

IBM Benchmark Tests

In order to test the IBM frame work for turbulent flow, DNS simulations are performed for fully developed channel flow and pipe flow where all essential scales of motion are resolved. The reasons to choose these two cases are: 1. Simple geometry; 2. Have turbulent flow characteristics; 3. Already well-studied with adequate experiment and simulation data available.

3.1 Channel Flow

Fully developed channel flow DNS simulation is carried out at $Re_\tau = 180$ based on half channel height δ^* and wall shear velocity u_τ^*. Simulation results are compared with [40] which has been used as the benchmark for turbulent channel flow.

The flow direction and the coordinate system are shown in Figure 3.1. Since the fully developed turbulent channel flow considered here is homogeneous in streamwise and spanwise directions, periodic boundary conditions are applied on these boundaries. The background mesh is shown in Figure 3.2. The background grid contains 278528 cells ($64 \times 68 \times 64$). The grid along the homogeneous X and Z direction is uniform, and a hyperbolic tangent distribution is used in the wall normal Y-direction is used. The distance of the first cell from the immersed surface is at $y^+ = 0.9$. To accommodate the immersed boundary in the Y direction, the background mesh domain in Y is slightly larger than the fluid domain height of 2.0 to make sure that there is an extra layer of cells outside the walls of the channel. Periodic boundary conditions are applied in the streamwise and spanwise directions. No slip boundary condition is applied at the immersed wall of the channel. Figure 3.3 shows the surface mesh used to define the walls of the channel which contains 8840 triangular surface elements. This surface mesh is located in the third interior cell in the Y-direction. A

constant heat flux boundary condition is also applied on the immersed surface. The extracted fluid IB nodes adjacent to the IB surface are shown in Figure 3.4.

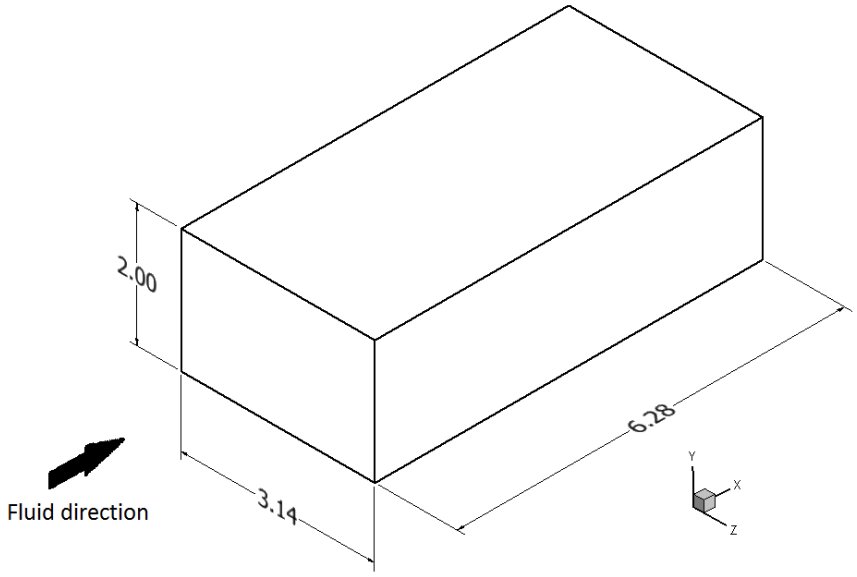

Figure 3.1: Flow direction, model dimension and coordinate system.

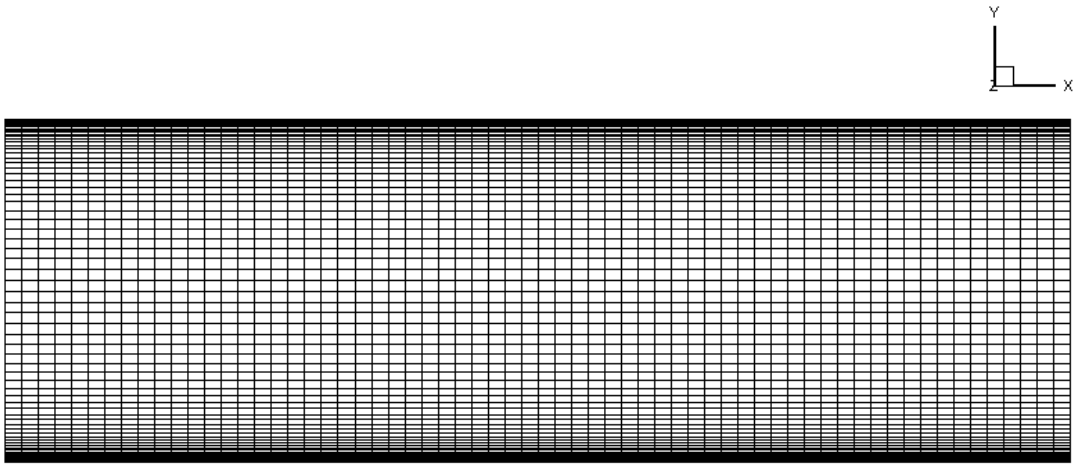

Figure 3.2: Background mesh.

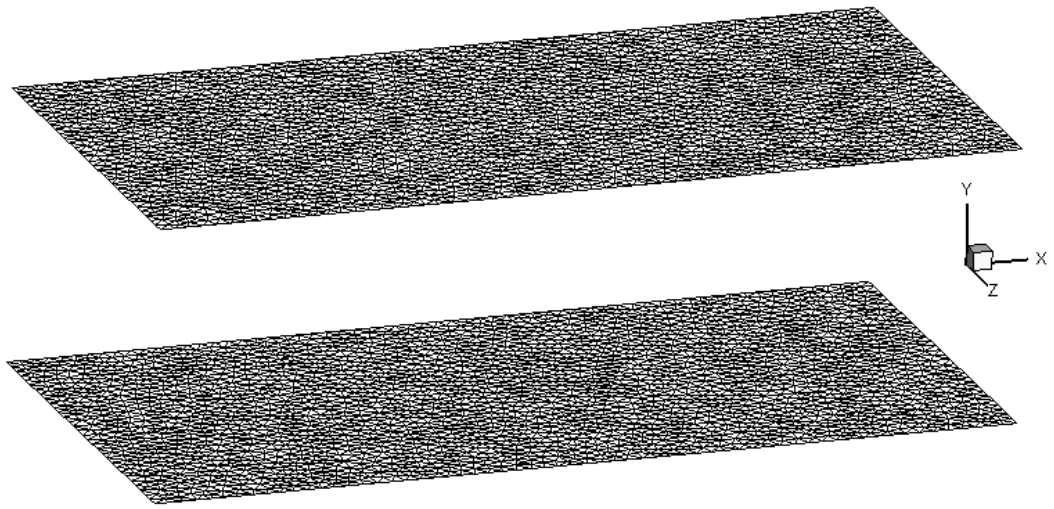

Figure 3.3: Surface mesh for XZ fluid domain.

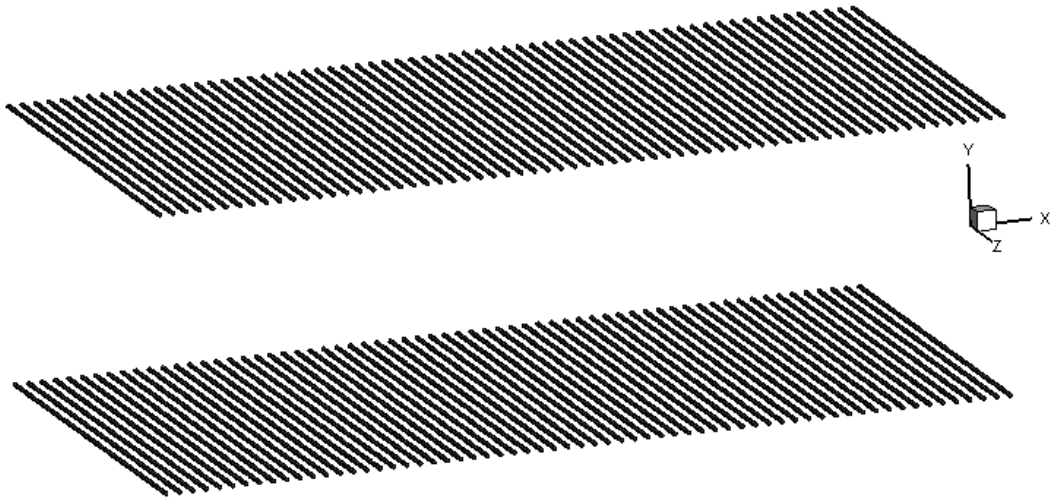

Figure 3.4: IB nodes formed in the background mesh.

As stated in Chapter 2, a mean pressure gradient source term is add in the flow direction (x direction) momentum equation. The simulation is initialized with a perturbed turbulent channel flow profile, which is allowed to develop in time till the flow reaches a steady state. The balance between the specified pressure gradient and wall friction will give a stationary mean velocity or flow rate.

Once a stationary flow rate is obtained, averaging to obtain the mean flow and turbulent statistics is initiated for 30 flow throughs in the x-direction.

Figure 3.5 shows the instantaneous iso-surface of coherent vorticity representative of the turbulence intensity in the channel flow (level= 13.54). The region close to the channel wall has much higher turbulent intensity than the center. Figure 3.6 shows the time averaged mean velocity profile. The IBM simulation results agree very well with Kim‘s DNS result. The maximum streamwise velocity is slightly under predicted by the IBM simulation, however the difference is still less than 1%. Turbulent root-mean-square velocity vs y+ is shown in Figure 3.7. The distribution of Urms and Vrms is captured with very good accuracy. However, Wrms is under predicted from y+ = 20 to 40, however the under prediction in peak value is less than 3.5%. Figure 3.8 presents the turbulent shear stress ($\overline{u'v'}$), the result from IBM also agrees well with the DNS results of Kim et al [40].

Table 3.1 contains the quantitative comparison among IBM, DNS of Kim et al [40]. and friction and heat transfer correlations from the literature. As stated before, the under predicted peak velocity value results from the over predicted wall shear stress which also accounts for the smaller Re_{D_h} and larger C_f. However, these differences are all around 1%. The averaged Nusselt number is obtained from a constant heat flux boundary condition applied on the immersed boundary. The agreement between IBM simulation and the Dittus-Boelter correlation is very good.

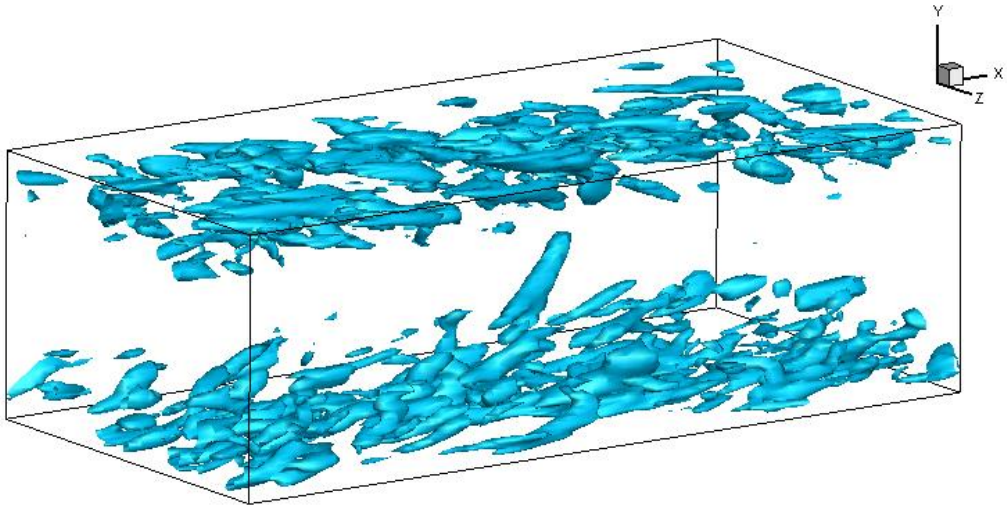

Figure 3.5: Instantaneous u_eigen (level=13.54).

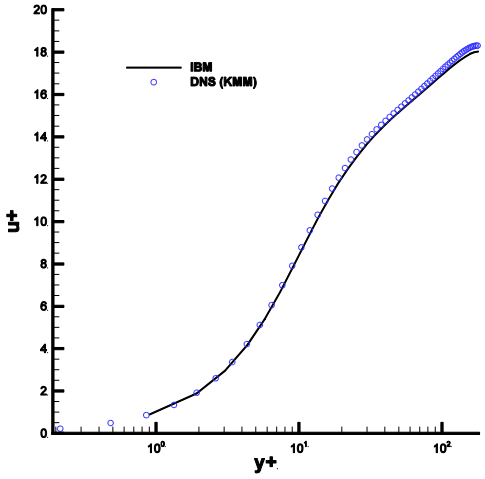

Figure 3.6: Time averaged velocity.

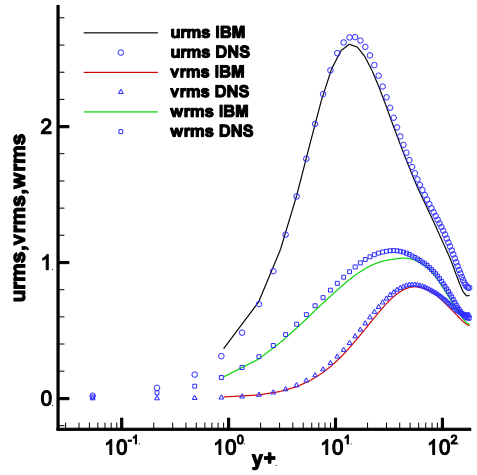

Figure 3.7: Turbulent statistics: Urms, Vrms, Wrms

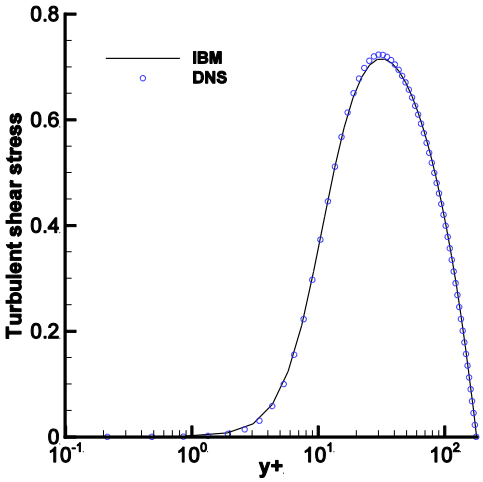

Figure 3.8: Turbulent shear stress.

Table 3.1: IBM results, bench mark DNS results and correlations.

	IBM	KIM ET AL.	CORRELATIONS (INCROPERA)
$Re_\tau = u_\tau^* \cdot \delta^* / \nu^*$	180	180	
$Re_{D_h} = u_m^* \cdot D_H^* / \nu^*$	11178	11200	
$C_f = \tau_w^* / (1/2) \cdot \rho^* \cdot {u_m^*}^2$	8.29×10^{-3}	8.18×10^{-3}	Petukhov : 8.18×10^{-3}
$Nu_{D_H} = h^* \cdot D_H^* / k^*$	36	-	Dittus-Boelter: 35.86

3.2 Pipe flow

Fully developed piped flow simulation is performed at $Re_\tau = 338$ based on pipe diameter D^* and wall shear velocity u_τ^*. Three different cases are tested: in Case 1, a body conforming grid is used which is the standard way of simulating the pipe flow; in Case 2, the immersed boundary method is used with a body conforming background grid; in Case 3, immersed boundary method is used with a Cartesian background grid. Numerical simulation data is compared with LDV experimental results[41]. All the experiment data has 0.3% uncertainty.

As stated in Chapter 2, a mean pressure gradient is added as a source term in the streamwise momentum equation to ensure the correctness of the streamwise periodic boundary condition. The derivation of this source term is shown below:

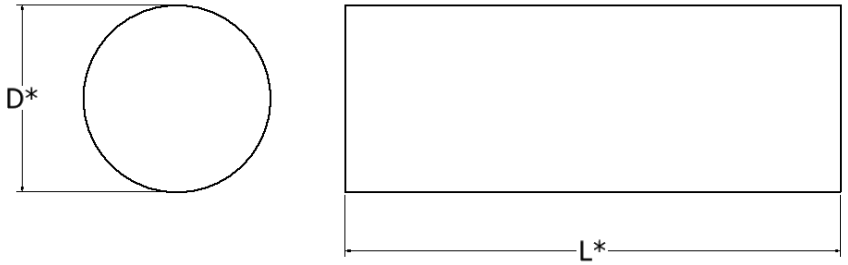

Figure 3.9: Pipe geometry.

From conservation of mean streamwise momentum:

$$\Delta P^* \left(\frac{\pi {D^*}^2}{4}\right) = {\tau_w}^* (\pi D^* L^*) \qquad \textbf{Equation 3.1}$$

Non-dimensionalizing by

$$\Delta P = \frac{\Delta P^*}{\rho^* u_\tau^{*2}}$$
$$u_\tau^* = \sqrt{\tau_{w_{eq}}^* / \rho^*} \qquad \textbf{Equation 3.2}$$

The dimensionless form of the mean pressure gradient is

$$\frac{\Delta P}{L} = 4 \qquad \textbf{Equation 3.3}$$

This $\frac{\Delta P}{L} = 4$ is added as a source term in the x-direction momentum equation.

The pipe geometry is shown in Figure 3.10. Periodic boundary condition is used in the x-direction with no-slip boundary conditions at the walls of the pipe.

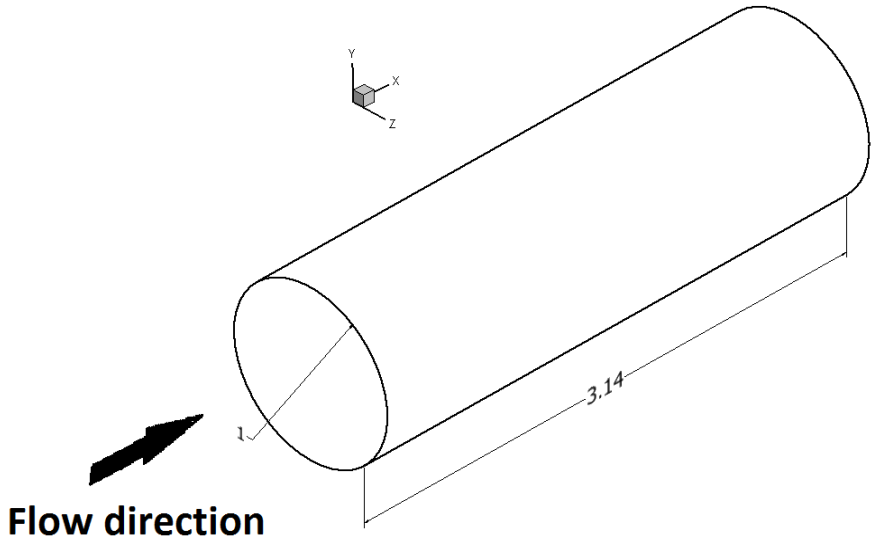

Figure 3.10: Simulation geometry, coordinate system and flow direction.

In Case 1, the body conforming grid is shown in Figure 3.11 and Figure 3.12. The domain is divided into 36 blocks, with $32 \times 40 \times 40$ cells per block for a total cell count of 1,843,200. The grid follows a hyperbolic distribution in the radial direction and uniform distributed in the circumferential and streamwise directions. The first cell Δ from the wall is 2.25×10^{-3} with $y^+ = 0.76$.

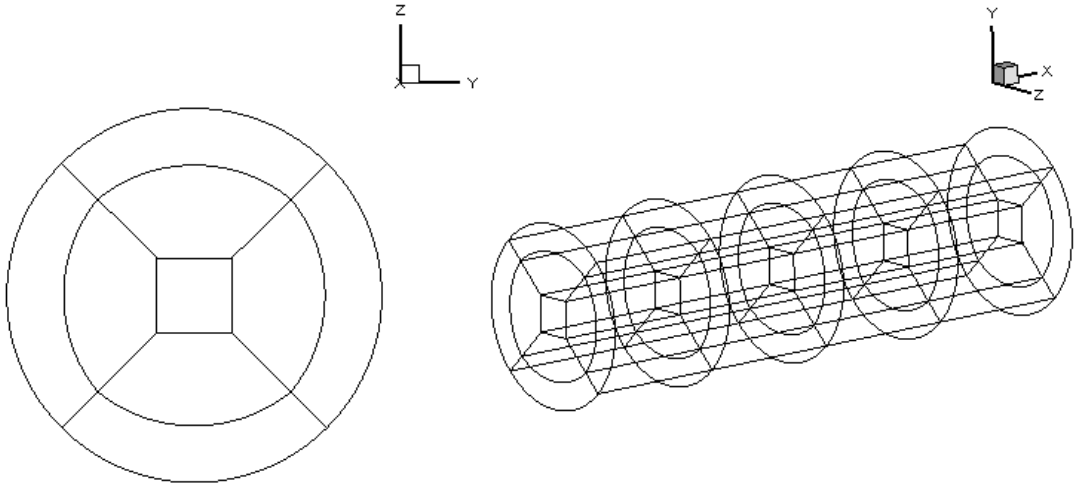

Figure 3.11: Body conforming mesh blocks.

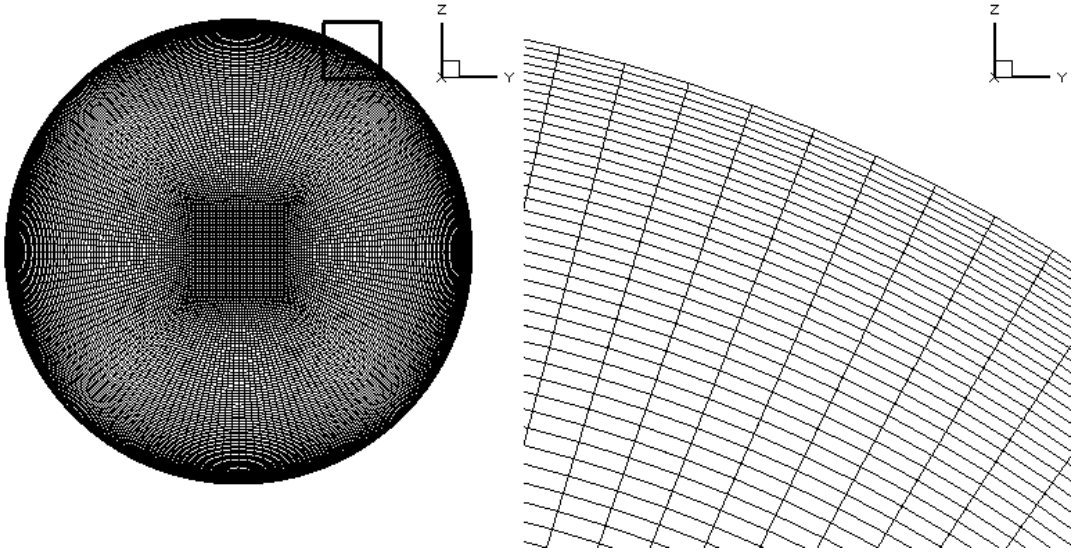

Figure 3.12: Body conforming grid (BCG).

In Case 2, a body conforming background grid is used along with the immersed boundary method. Figure 3.13 shows the background grid. The background grid has the same block configuration and total number of cells. The only difference is shown in Figure 3.14. This background grid has a diameter $D^* = 1.05$ which is 0.05 larger than the grid used in Case 1. This larger diameter allows 2 extra layers of cell to lie outside the immersed surface to form the solid boundary for the fluid domain. The two layers of larger cells is shown in Figure 3.14, with the immersed surface located at the third layer from the wall. The immersed surface mesh used in this case is shown in Figure 3.15. This surface mesh contains 230,940 triangle unstructured cells, which form a $D^* = 1.0$ cylindrical surface. Periodic boundary condition is applied in the x-direction, and the immersed surface has no-slip wall boundary condition.

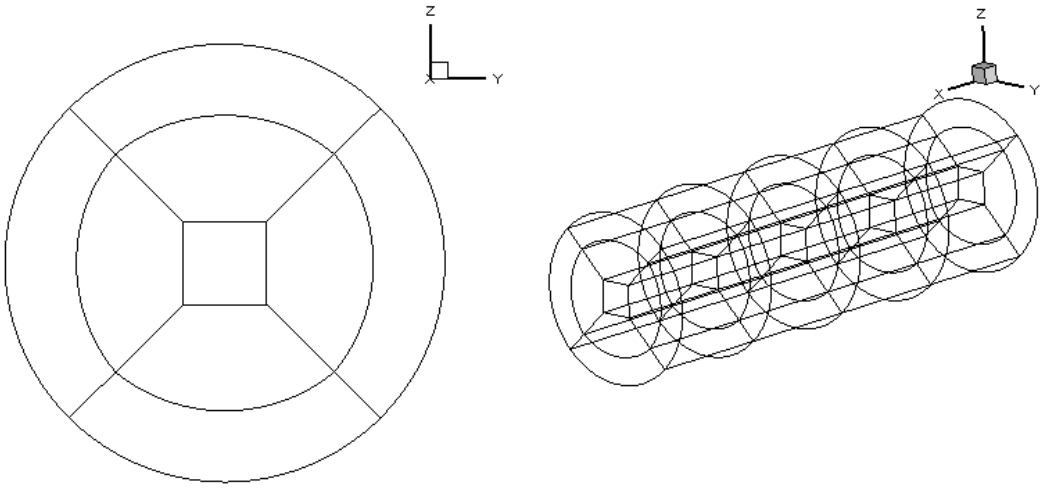

Figure 3.13: Body conforming background grid block for IBM.

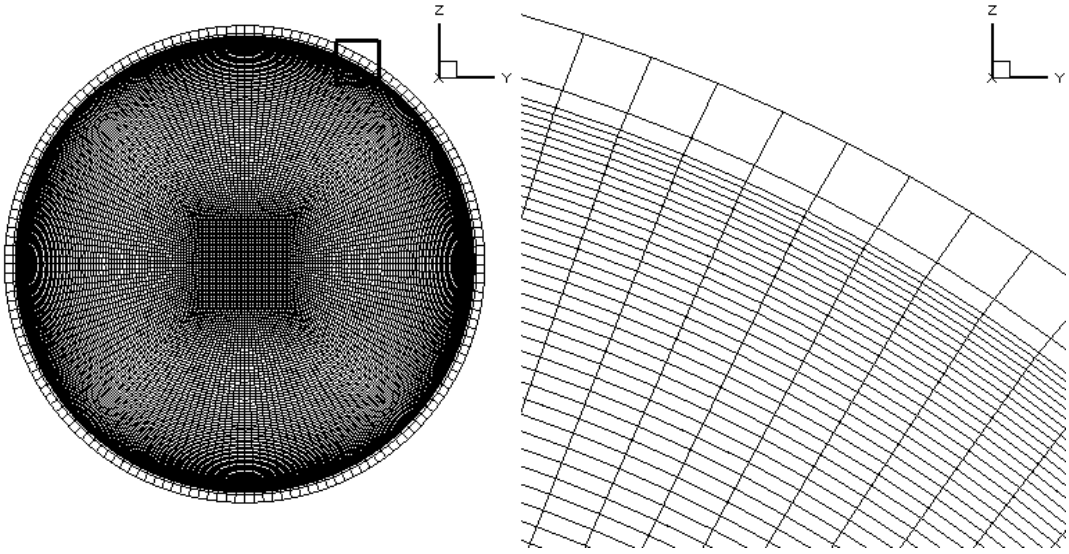

Figure 3.14: Body conforming background grid for IBM.

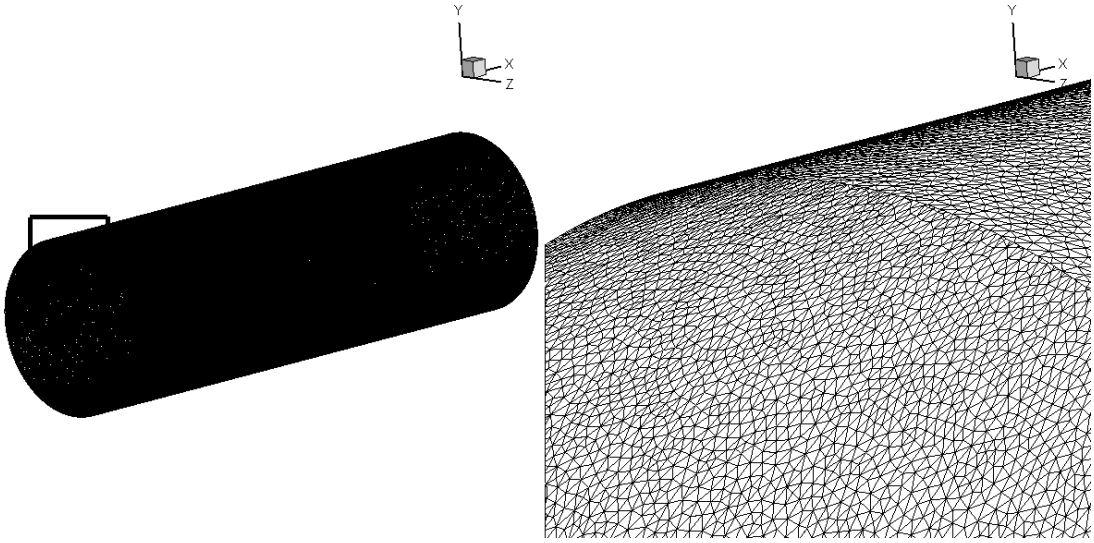

Figure 3.15: Surface mesh for IBM cases.

In the third case, Case 3, a Cartesian grid is used as the background mesh. The grid is divided into $4 \times 8 \times 8$ blocks, $25 \times 50 \times 50$ cells in each block, for a total 16,000,000 cells, shown in Figure 3.16. Note that in this case, unlike a body conforming grid, a non-uniform grid distribution is not viable in the cross-section, and a fine uniform grid has to be used to capture the inner layer turbulent scales. The cell size in the cross-section is dictated by the near wall resolution requirement and is 2.625×10^{-3}, which equals $y^+ = 0.887$. Periodic boundary condition is applied in the x-direction, and the side faces are no-slip solid wall boundary condition. The surface mesh is the same as that used in Case 2.

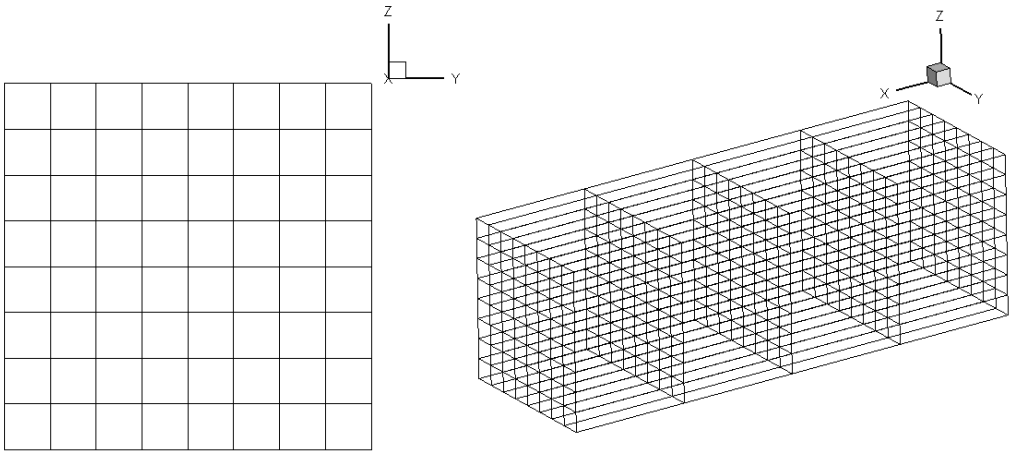

Figure 3.16: Cartesian background mesh block for IBM

Figure 3.17 shows the time averaged velocity profile. The agreement among BCG, BCG with IBM, and experiment is very good. IBM with Cartesian grid under predicts the velocity near the central region of the pipe, however the difference compared to the experiment data is under 2%.

Figure 3.18. shows the rms values of the u (streamwise) velocity fluctuation (Urms). The overall prediction of BCG, BCG with IBM, and IBM with Cartesian grid agrees very well with the experiment data. These simulations accurately capture the Urms distribution along y^+, except for a slight under prediction of the peak value at $y^+ = 10.5$.

In Figure 3.19, the rms of the radial direction velocity (Vrms) is plotted against y^+. The numerical prediction agrees well with the experiment when y^+ is larger than 10. The simulation prediction of Vrms differs significantly from the experiment between $y^+ = 3$ to $y^+ = 10$. The reason for this underestimation remains unclear. One possible explanation is that the normal velocity in the near-wall region is very hard to measure. The quantity is extremely sensitive to measurement noise [41] which leads to large Vrms value observed in the near-wall region from the experiment.

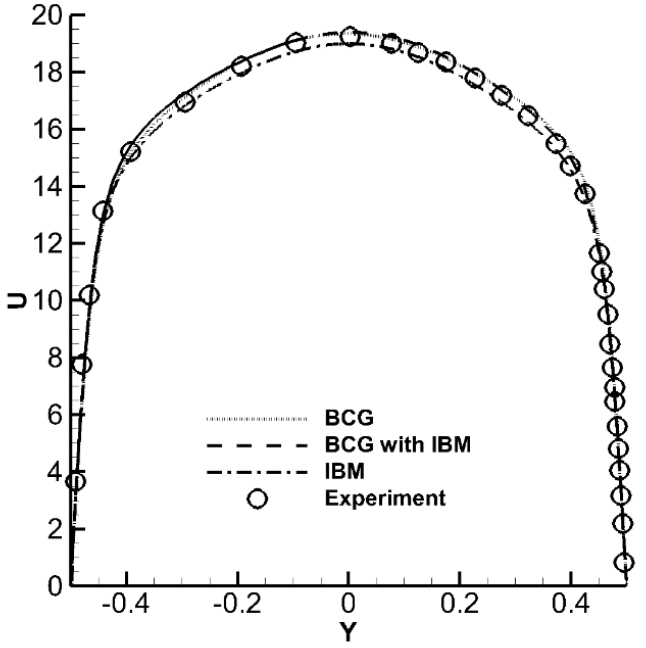

Figure 3.17: Time averaged streamwise velocity.

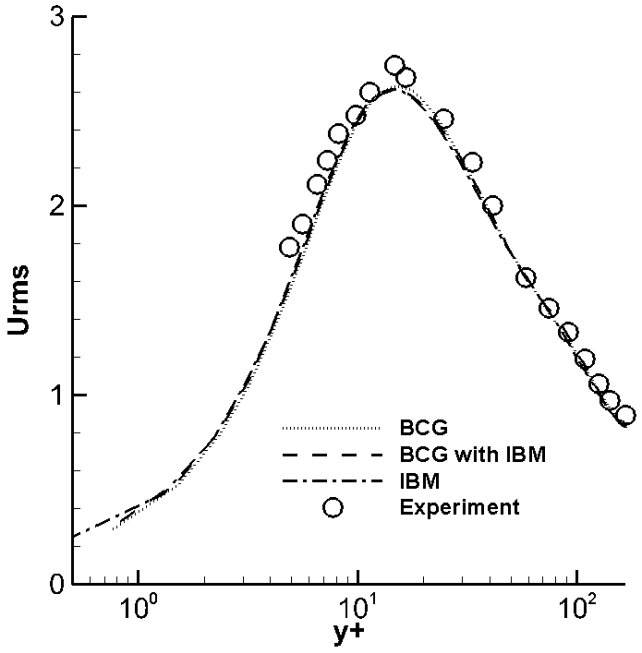

Figure 3.18: Turbulent statistics, Urms.

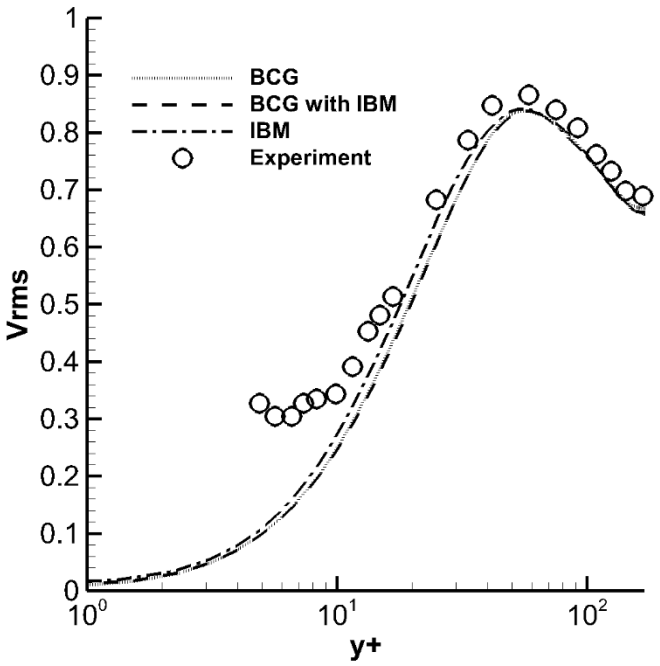

Figure 3.19: Turbulent statistics, Vrms.

The turbulent shear stress is given in Figure 3.20. The agreement is quite reasonable. In the $Y = 0.2$ to $Y = 0.35$ region, the simulation cases show some differences among each other. The IBM with Cartesian case seems to agree the best with experiment, whereas the other two simulation cases BCG and BCG with IBM have very reasonable predictions. The overall difference between the simulations and experiment is very small in the whole region.

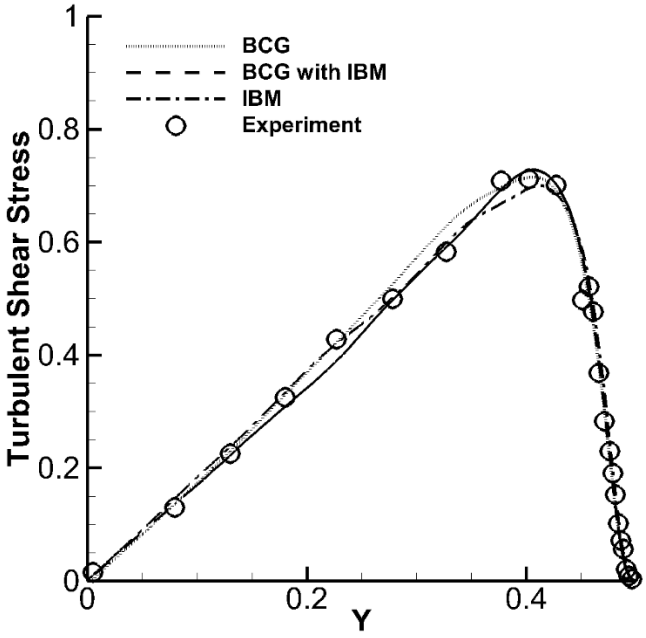

Figure 3.20: Turbulent shear stress (experiment error 0.3%).

3.3 Conclusion

In this chapter, immersed boundary method frame work is tested for turbulent flow. DNS simulation is performed for two benchmark test cases: fully developed channel flow and pipe flow.

IBM simulation data are compared with well-accepted DNS results for channel flow and with LDV measurements in pipe flow. These comparisons show that IBM can capture the flow characteristics as accurately as the traditional body conforming grid methods.

Moreover, in the pipe flow case, although the difference in flow predictions is small between IBM with BCG and IBM with Cartesian grid, the computational cost difference is significant. IBM with Cartesian grid has 16,000,000 cells, by contrast, IBM with BCG only has 1,843,200 cells. The

computation cost savings by using BCG with IBM suggests that in many cases it might be advantageous to use BCG to map external boundaries, using the IBM for internal immersed surfaces which might be difficult to grid within the framework of the BCG.

Chapter 4

IBM Ribbed Duct Tests

After evaluations of the accuracy of Immersed Boundary Method (IBM) in turbulent channel flow and pipe flow, IBM is further investigated in ribbed duct geometry used in internal cooling passages of gas turbine blades. Two geometries are tested: Case 1, an orthogonal non-staggered ribbed duct is simulated at $Re = 20{,}000$. Velocity field, turbulent statistics and Nusselt number from IBM predictions are compared with body conforming grid simulation results [42]; Case 2, a one side ribbed duct is simulated at $Re = 15{,}000$ and under 3 rotation numbers: Ro $= 0.3$, Ro $= -0.3$ and Ro $= 0.0$ (stationary). For these cases, the simulation results are compared with PIV experiment data [16]. The dynamic Smagorinsky subgird stress model is used with a second-order central difference discretization for these two cases. This is a first study where IBM is used to capture the geometry with sharp corners and simulate complex three dimensional flow, and the study is also a very necessary step to validate IBM before applying it to more complex geometries like the cooling passage shown in Chapter 1. These two test cases show that with IBM captures the geometry features, the predictions have very good accuracy when compare to traditional BCG simulation and PIV experiment data.

4.1 Orthogonal non-staggered ribbed duct

4.1.1 Computational domain

Figure 4.1 shows the orthogonal non-staggered ribbed duct geometry and coordinate system. The rib height to hydraulic diameter ratio, e/D_h, is 0.1 and rib pitch to rib height ratio, p/e, is 10. Flow is simulated under the fully developed assumption at $Re = 20{,}000$. Reynolds number is

calculated based on: $= \frac{U_0 D_h}{v}$, u_0 is the reference fluid velocity, D_h is the characteristic length scale (the channel hydraulic diameter), and v is the kinematic viscosity. Periodic boundary condition is applied in streamwise (x) direction and all the walls of the duct and the ribs are treated as no-slip boundaries with constant heat flux. The calculation was run for about 50 flow through time units with mean and turbulent statistics calculated for the last 20 units.

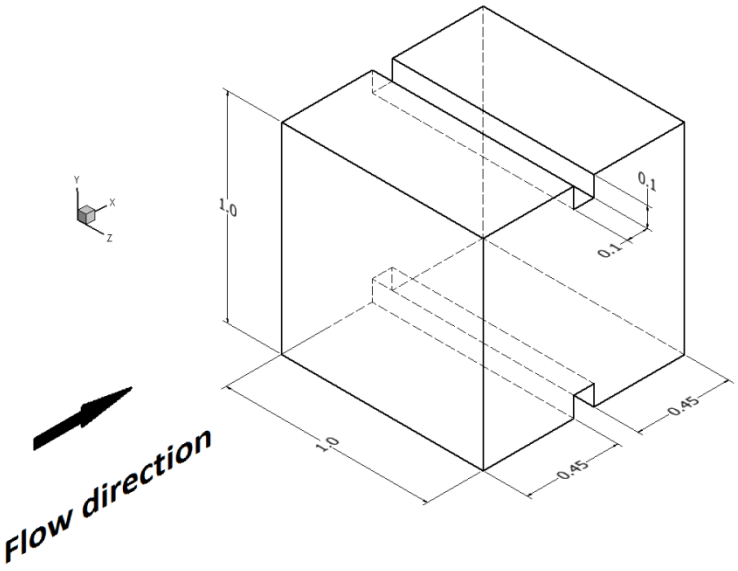

Figure 4.1: Computational domain and coordinate system.

Figure 4.2 shows the background grid. The grid is $128 \times 136 \times 136$ in the x, y and z-direction, and follows a hyperbolic tangent distribution near the wall boundary. The grid size near the IB surface is 2.5×10^{-4} which ensures the Y+ of the fluid IB nodes smaller than 1. In y and z-direction, the size of the background grid is slightly larger than the computational domain which allows extra layers of grid cells located outside the IB surface. Figure 4.3 shows the surface mesh used to define the duct wall and rib wall which contains 2.8 million unstructured triangular surface elements. The fluid IB nodes adjacent to rib and duct surfaces are shown in Figure 4.4.

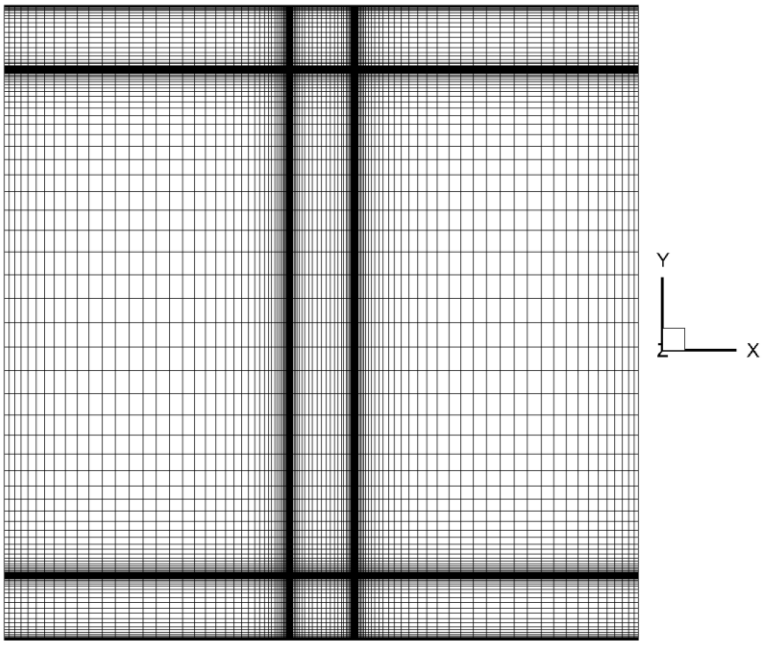

Figure 4.2: Backgournd mesh.

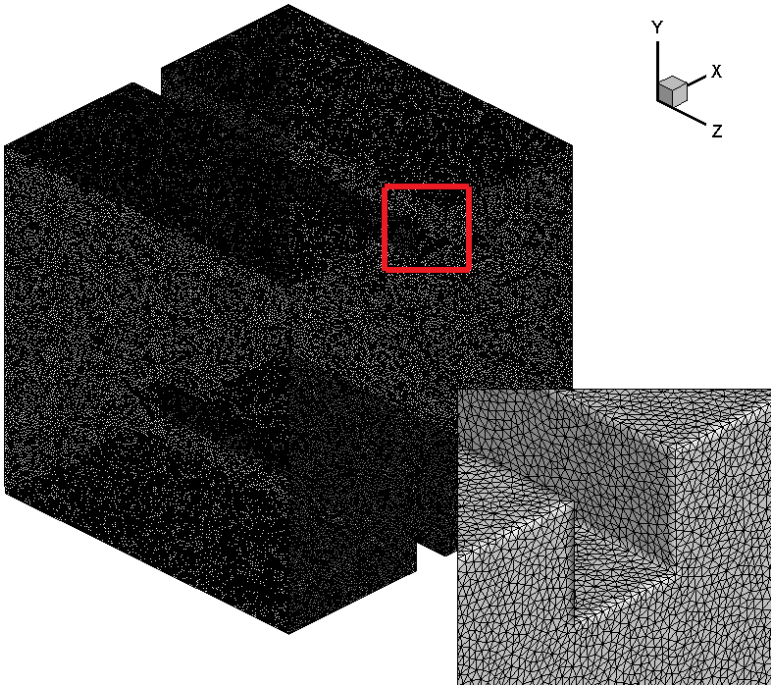

Figure 4.3: Surface grid.

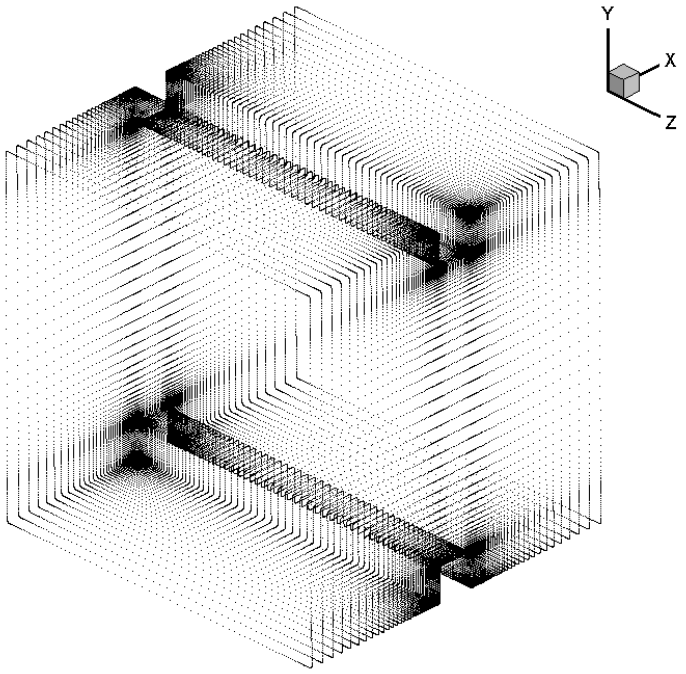

Figure 4.4: Fluid IB node adjacent to rib and duct surfaces.

4.1.2 Results and discussion

Figure 4.5 shows the mean streamline distribution at the center plane of the duct (z=0.5). The blockage effect of the rib causes the flow to accelerate at the rib and to expand suddenly after it. The incoming boundary layer is forced to separate when approaching the front side of the rib, and a time averaged clockwise-rotating corner vortex is formed at the rib-wall junction. The shear layer formed on the front face of the rib separates at the upstream edge as part of it attaches back on the rib top producing a small recirculating zone on top of the rib. This shear layer separates again at the downstream edge of the rib forming a large time-averaged recirculation bubble behind the rib. The near wall flow of the primary recirculation, separates creating a secondary corner vortex at the back side of the rib-wall junction, rotating counter-clockwise. The shear layer which separates from the top surface of the rib reattaches on the inter-rib duct surface after the bubble, and a new boundary layer

develops from this point and separates again when approaching the next rib. IBM predicts the reattachment point at about 4 rib height from the rib back surface. As shown in Figure 4.5, IBM captures all the major features of the flow.

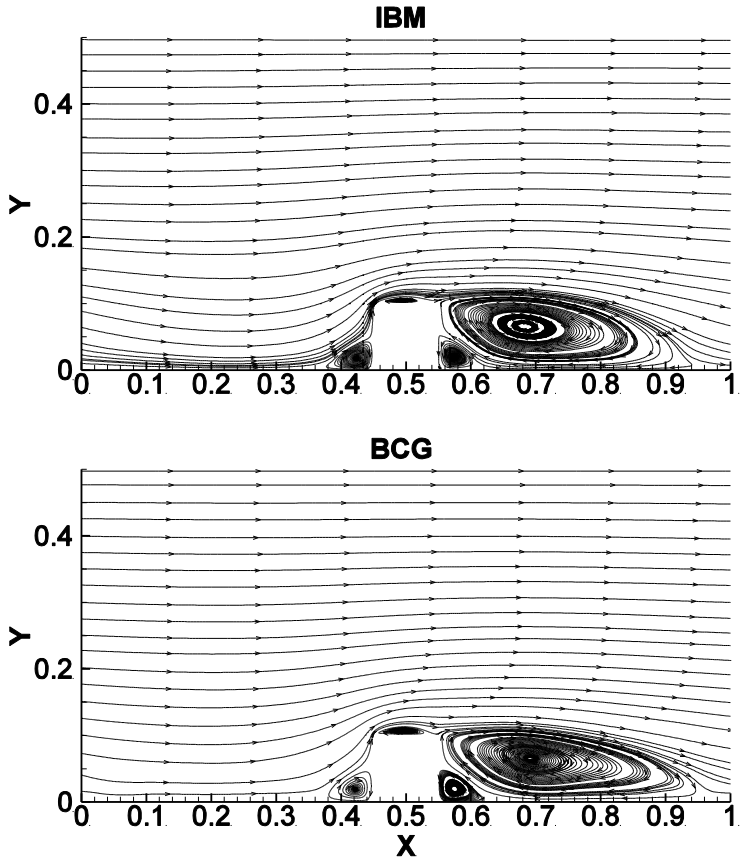

Figure 4.5: Mean flow streamline distribution in the z-symmetry (z=0.5) plane.

Figure 4.6 to Figure 4.9 represent the contours of time averaged turbulent statistics: u_{rms}, v_{rms}, w_{rms} (normalized by the bulk mean velocity) and shear stress $-\overline{u'v'}$ (normalized by the square of the bulk mean velocity) at the center plane of the duct ($z = 0.5$). In Fig. the maximum value of u_{rms} is around 50%, located at the leading edge of the rib where the shear layer starts to separate. The lowest value is located in the stagnating flow at the rib-wall junction corner and in the recirculation region immediately behind the rib. IBM agrees very well with BCG results in the near-wall and near rib

region (Y<0.25), and over predicts u_{rms} by 5% near the center of the duct (y>0.3). The transverse fluctuations v_{rms} at the center plane (z=0.5) is shown in Figure 4.7. v_{rms} is around 25% in the stagnation region of the rib and in the separated shear layer downstream of the rib and 12% in the middle. The prediction values of IBM compare to BCG is very good near the rib and over predicted by 2%~3% in the center region. The lateral fluctuations w_{rms} at the center plane (z=0.5) is presented in Figure 4.8. The maximum value is 40% which occurs at the leading edge of the rib. High span wise intensities are observed because of the impingement of eddies at the leading edge of the rib. The w_{rms} is also high in the shear layer downstream of the rib with a maximum value of about 35%. This phenomenon is further explained in detail by Tafti [2006]. Time averaged Reynolds shear stress $-\overline{u'v'}$ is shown in Figure 4.9. The maximum value -5% is located in the separated shear layer downstream of the rib. IBM predictions have very good agreement with BCG.

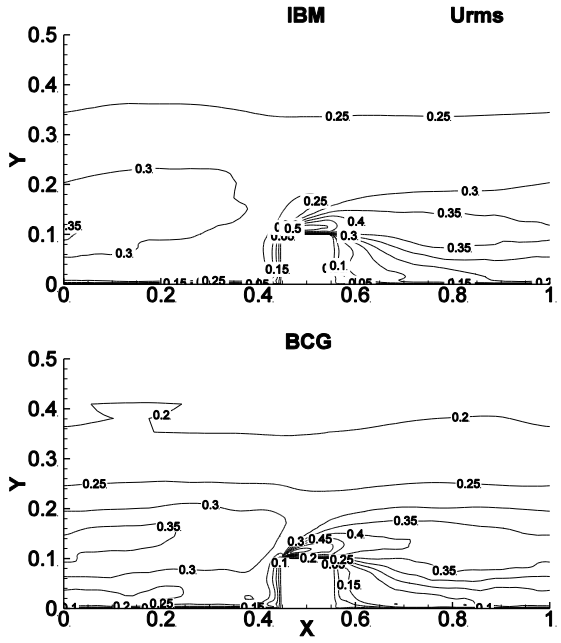

Figure 4.6: Turbulent statistics, Urms at center plane (z=0.5).

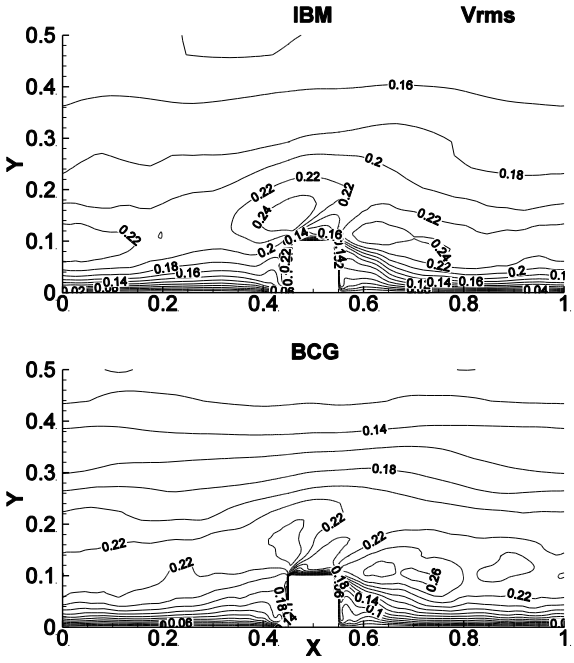

Figure 4.7: Turbulent statistics, Vrms at center plane (z=0.5).

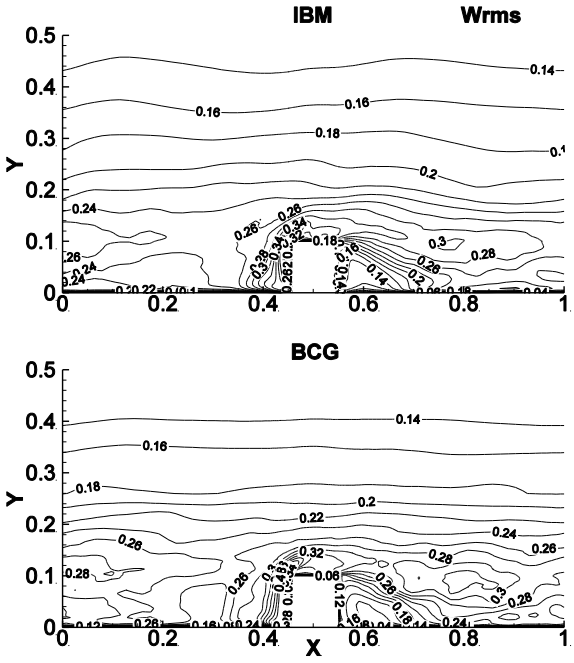

Figure 4.8: Turbulent statistics, Wrms at center plane (z=0.5).

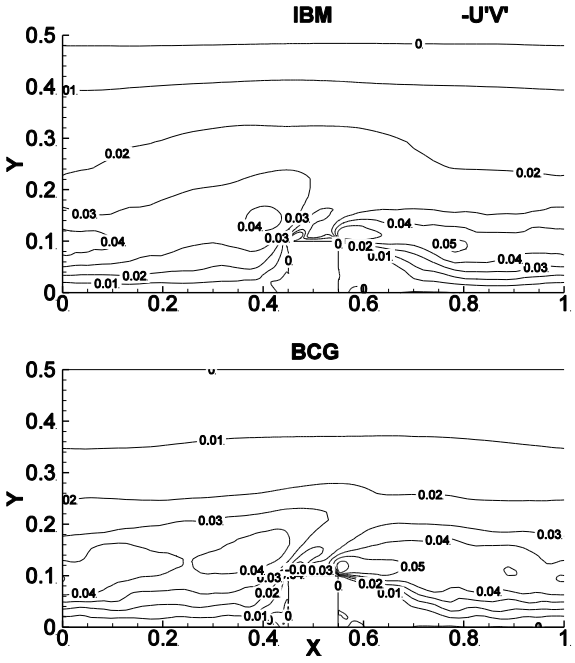

Figure 4.9: Distribution of turbulent shear stress at center plane (z = 0.5).

Figure 4.10 shows the turbulent statistics at x=1, z=0.5 (center line between two ribs). As stated before, IBM captures the peak value of u_{rms} and v_{rms} with very good accuracy except for slight over prediction at the center region of the duct. For w_{rms} and $-\overline{u'v'}$, the overall IBM results exhibit good agreement with BCG data but under predicts the peak value of $-\overline{u'v'}$.

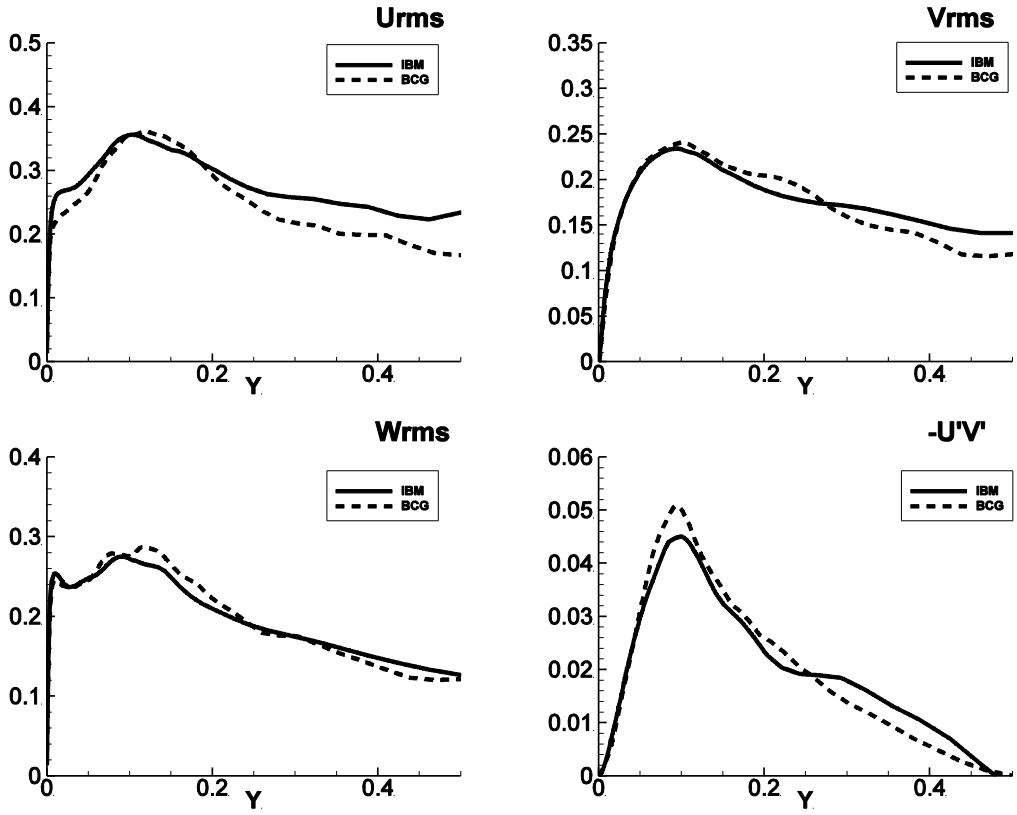

Figure 4.10: Turbulent statistics at X = 1, Z = 0.5.

Figure 4.11 shows the Nusselt number augmentation (Nu/Nu_0) distribution from IBM calculation. The augmentation ratio is calculated based on the Dittus-Boelter correlation, $Nu_0 = 0.023 \cdot Re^{0.8} \cdot Pr^{0.4}$. On the smooth wall, higher heat transfer augmentation is observed in the vicinity of the rib junction, shown in Figure 4.12. This is because the highly unsteady vortical structures induced by the rib-wall junction that impinge on the smooth wall making the flow highly 3D in this region. IBM predictions agrees very well with the BCG results. On the rib wall, shown in Figure 4.13, the peak augmentation is located at the upstream corner of the rib-wall junction where highly unsteady secondary junction eddies are produced. The region immediately after the rib, in the corner recirculation region, the augmentation is small due to low turbulence intensities. The augmentation

increases to 3~3.5 in the primary recirculation region where the shed vortices from the rib reattach on the ribbed wall. IBM slightly under predicts the augmentation near the middle part of the rib. Figure 4.14 shows the augmentation on the rib surfaces. On the upstream face (rib front), heat transfer coefficient reaches the maximum value 5 at the leading edge as a result of high flow velocity. The augmentation is about 3.5 at the rib top due to the small recirculation zone formed by the separated shear layer. On the rib back, the augmentation is about 1 to 2. IBM captures all the mean nusselt distributions on the rib surface, but slightly under predicts the augmentation near the middle part of the rib on rib front and rib top surface.

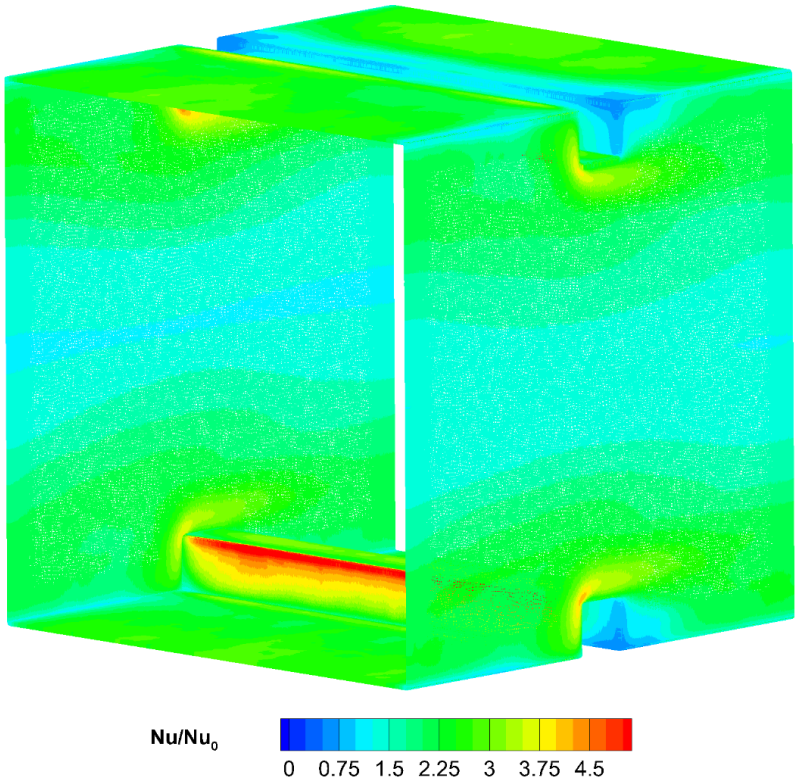

Figure 4.11: Contour of Nusselt number augmentation distribution from IBM.

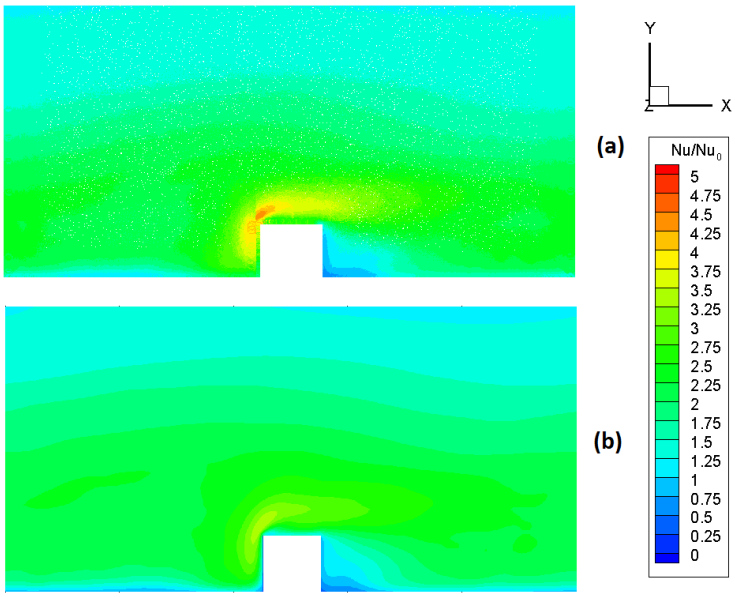

Figure 4.12: Contour of Nusselt number augmentation distribution on smooth wall: (a) IBM ,(b) BCG.

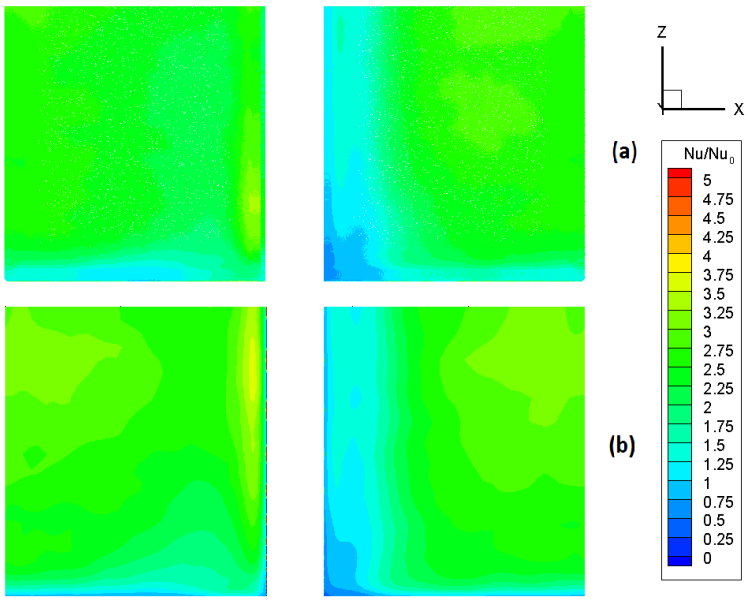

Figure 4.13: Contour of Nusselt number augmentation distribution on rib-wall (from z=0 to z=0.5): (a) IBM ,(b) BCG.

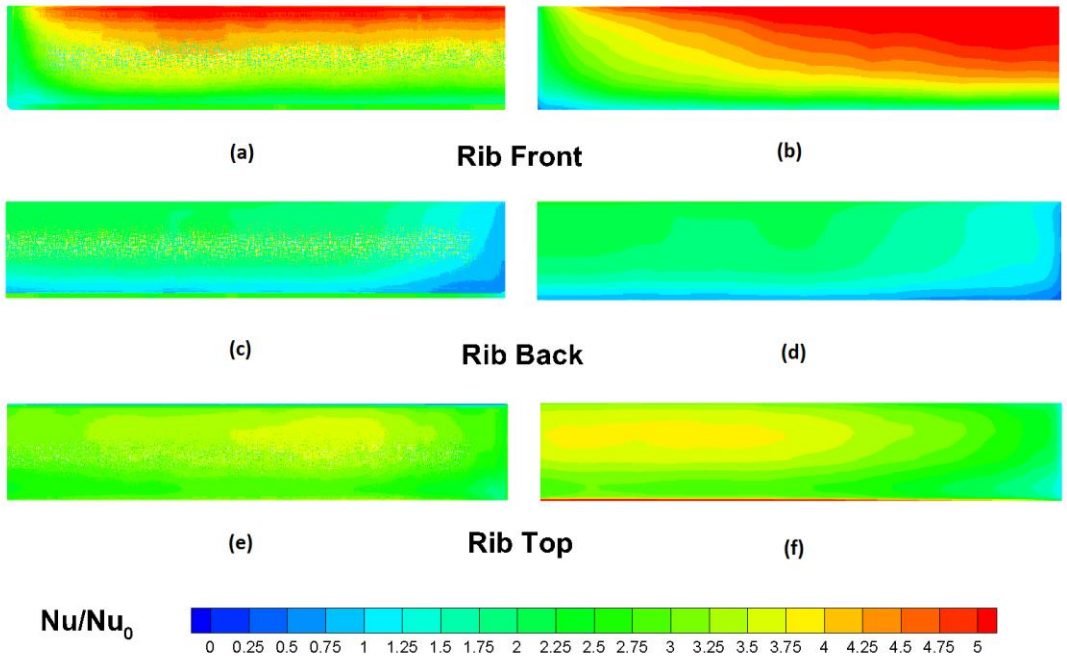

Figure 4.14: Contour of Nusselt number augmentation distribution on rib surface (from z=0 to z=0.5): IBM (a)(c)(e); BCG (b)(d)(e).

4.2 One side ribbed duct

Rotational Coriolis forces have a large influence on the flow structure in the duct. In the current configuration, the ribbed wall acts as the trailing side for $Ro = 0.3$, and the leading side for $Ro = -0.3$. Because of rotation, the flow is pushed to the trailing side of the duct establishing a pressure gradient in the cross-section of the duct. The pressure gradient leads to secondary flows which typically impinge on the trailing side of the duct creating an upwash region along the side walls. Coriolis forces also have a direct effect on the production of normal and shear turbulent stresses. On the trailing side, Coriolis forces enhance the turbulent production mechanism while attenuating production on the leading side. The mean flow is pushed towards to the rib wall and the

reattachment length is decreased. The secondary flows induced by Coriolis force are shown in Figure 4.15.

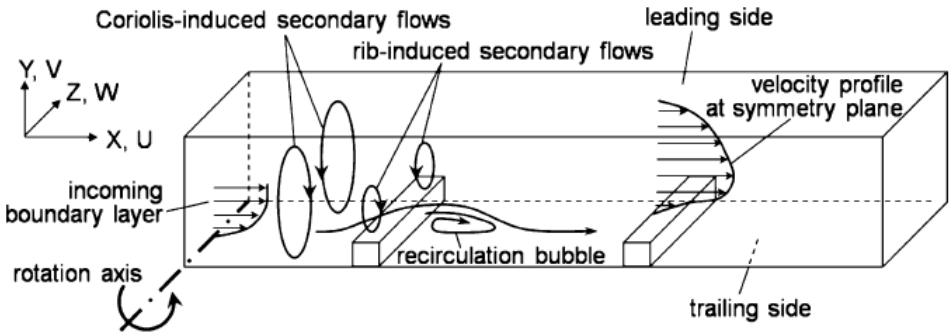

Figure 4.15: Schematic view of secondary flows in the rotating ribbed duct [16].

4.2.1 Geometry and computational grid

Figure 4.16 shows the one side ribbed duct geometry, coordinate system and rotation direction. The rib height to hydraulic diameter ratio, e/D_h, is 0.1 and rib pitch to rib height ratio, p/e, is 10. Flow is simulated under the fully developed assumption under three different rotation number: $Ro = 0.3$, $Ro = -0.3$ and $Ro = 0$ (stationary) at $Re = 15{,}000$. Reynolds number is based on the bulk velocity and hydraulic diameter of the cross section. Rotation is applied along the z direction. Rotation number is calculated by $Ro = \frac{\Omega D_h}{U_0}$, Ω is the angular velocity about the z-axis, D_h is the hydraulic diameter, U_0 is the bulk velocity. Periodic boundary condition is applied in streamwise (x) direction and all the walls of the duct and the ribs are treated as no-slip boundaries with constant heat flux. The calculation was run for about 30 flow through time units with mean and turbulent statistics calculated for the last 16 units.

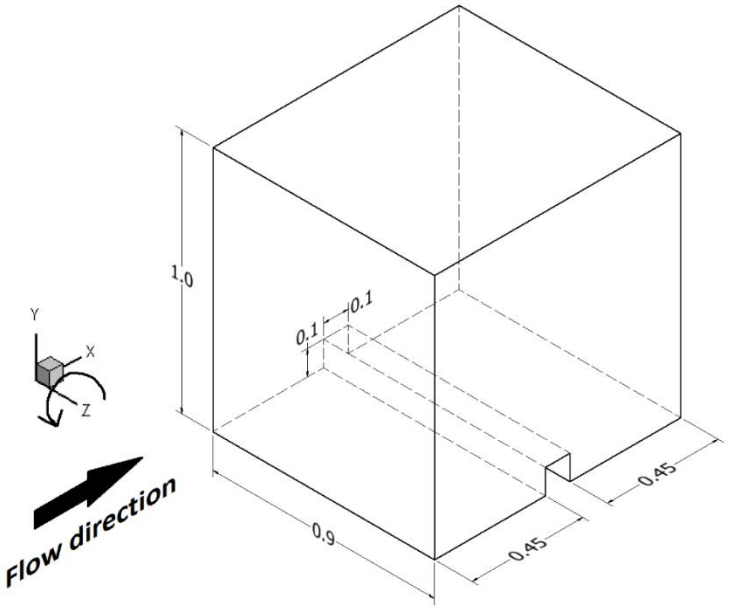

Figure 4.16: Computational domain and coordinate system.

The background mesh is shown in the Figure 4.17. It contains $128 \times 136 \times 136$ in x, y and z direction, and follows a hyperbolic tangent distribution near the wall and rib surface. The grid size near the IB surface is 2.5×10^{-4} which ensures the Y+ of the fluid IB nodes smaller than 1. In y and z-direction, the size of the background grid is slightly larger than the computational domain which allows extra layers of grid cells to lie outside the IB surface and can be identified as solid nodes. The surface mesh which contains 1.4 million unstructured triangle cells is shown in Figure 4.18. Figure 4.19 shows the fluid IB nodes adjacent to rib and duct surfaces.

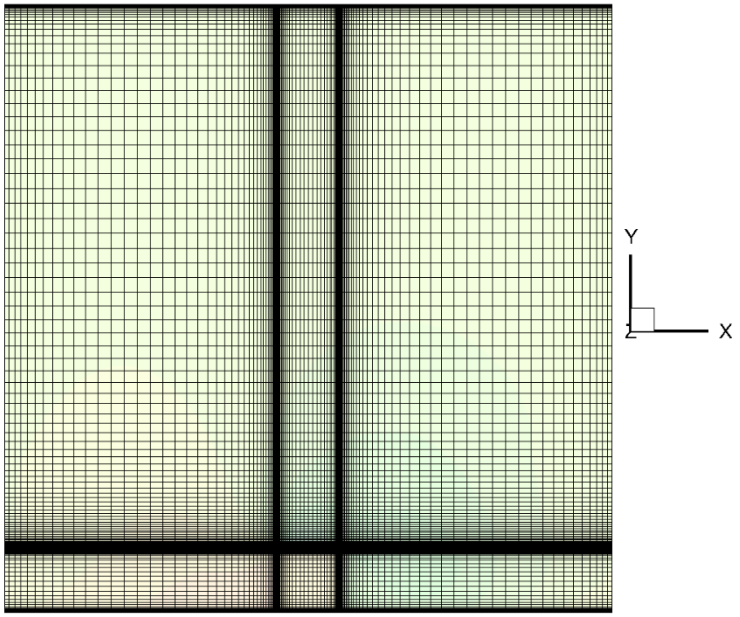

Figure 4.17: Background mesh.

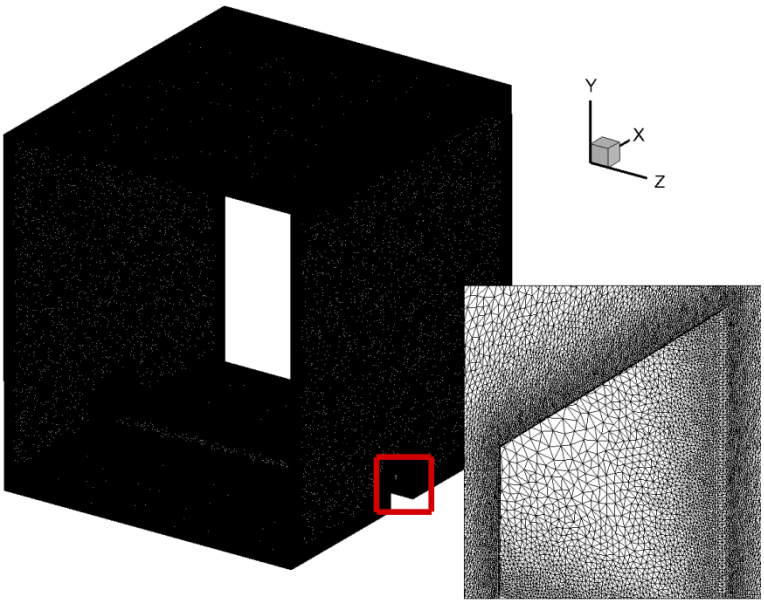

Figure 4.18: Surface mesh.

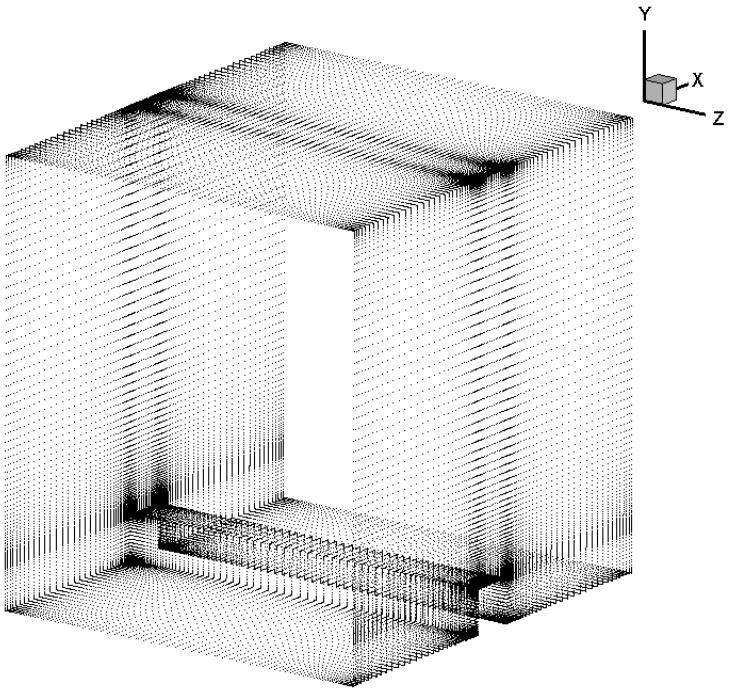

Figure 4.19: Fluid IB node adjacent to rib and duct surfaces.

4.2.2 Results and discussion

4.2.2.1 Mean velocity fields

Figure 4.20 shows the time-averaged two-dimensional streamlines and contours of velocity magnitude distribution at center plane z=0.45. In the stationary case, Figure 4.20 (b) and (e), the blockage effect of the rib causes the flow to accelerate at the rib and to expand suddenly after it. The incoming boundary layer is forced to separate when approaching the front side of the rib, and a time averaged clockwise-rotating corner vortex is formed at the rib-wall junction. The shear layer formed on the front face of the rib separates at the upstream edge as part of it attaches back on the rib top producing a small recirculating zone on top of the rib. This shear layer separates again at the

downstream edge of the rib forming a large time-averaged recirculation bubble behind the rib. The near wall flow of the primary recirculation, separates creating a secondary corner vortex at the back side of the rib-wall junction, rotating counter-clockwise. The shear layer which separates from the top surface of the rib reattaches on the inter-rib duct surface, and a new boundary layer develops from this point and separates again when approaching the next rib. The reattachment point is observed at 4.2e from the trailing edge of the rib. As shown in Figure 4.20, IBM captures all the major features of the flow.

In the stabilizing rotation case, the shear layer doesn't separate on top of the rib. The small recirculating zone in front of the rib and the primary recirculation after the rib are much larger compared to the stationary case. This is due to the stabilizing effect of Coriolis forces. In both IBM and BCG simulation, in Figure 4.20 (a) and (d), the primary recirculation bubble adjoins the corner vortex in front of the next rib. The shear layer separates at the trailing edge of the rib and doesn't reattach to the wall until it reaches the leading surface of the next rib, leaving no reattachment point between the ribs. This phenomena observed in numerical simulation is different from the experiment. In Figure 4.21 (a) of the PIV experiment results[16], the primary recirculation zone is smaller, and they conclude that a reattachment point is observed at 5.65e from the trailing surface of the rib.

In the destabilizing rotation case, Figure 4.20 (c) and (f), the Coriolis-induced secondary flows push the flow from the central part of the duct to the rib wall. This secondary flow together with the Coriolis force shrinks the primary recirculation bubble behind the rib and the corner vortex in front of the rib. The reattachment point is observed at 3.5e from the trailing surface of the rib.

The velocity magnitude is also affected by the rotation, contours shown in Figure 4.20. In the stabilizing rotation, the Coriolis force pushes the flow away from the rib wall, leaving flow with low velocity near the rib wall. The velocity magnitude at Y/e=3 plane is about 0.9 in stabilizing rotation

while in stationary case is about 1.0. In the destabilizing case, the Coriolis effect is opposite which pushes the flow from the center towards the rib wall which results in a higher velocity field near the rib wall.

Comparing to the BCG method, IBM predicts nearly identical results. IBM marginally over predicts the velocity magnitude near the center of the duct. Comparing to the PIV experiment data, Figure 4.21, both IBM and BCG capture all the flow features in stationary and destabilizing rotation cases. The disagreement in the reattachment point has already been mentioned before. In the experiment plot shown in Figure 4.21 (a), the streamline shown in the figure doesn't indicate a very clear reattachment point, and the author doesn't present the method they used to measure this point other than looking at the streamline. Therefore, the reattachment point in stabilizing rotation in the experiment needs further study. The reattachment length observed by IBM, BCG and experiment is shown in Table 4.1. More details about how the Coriolis forces affect the reattachment length can be found in reference [30].

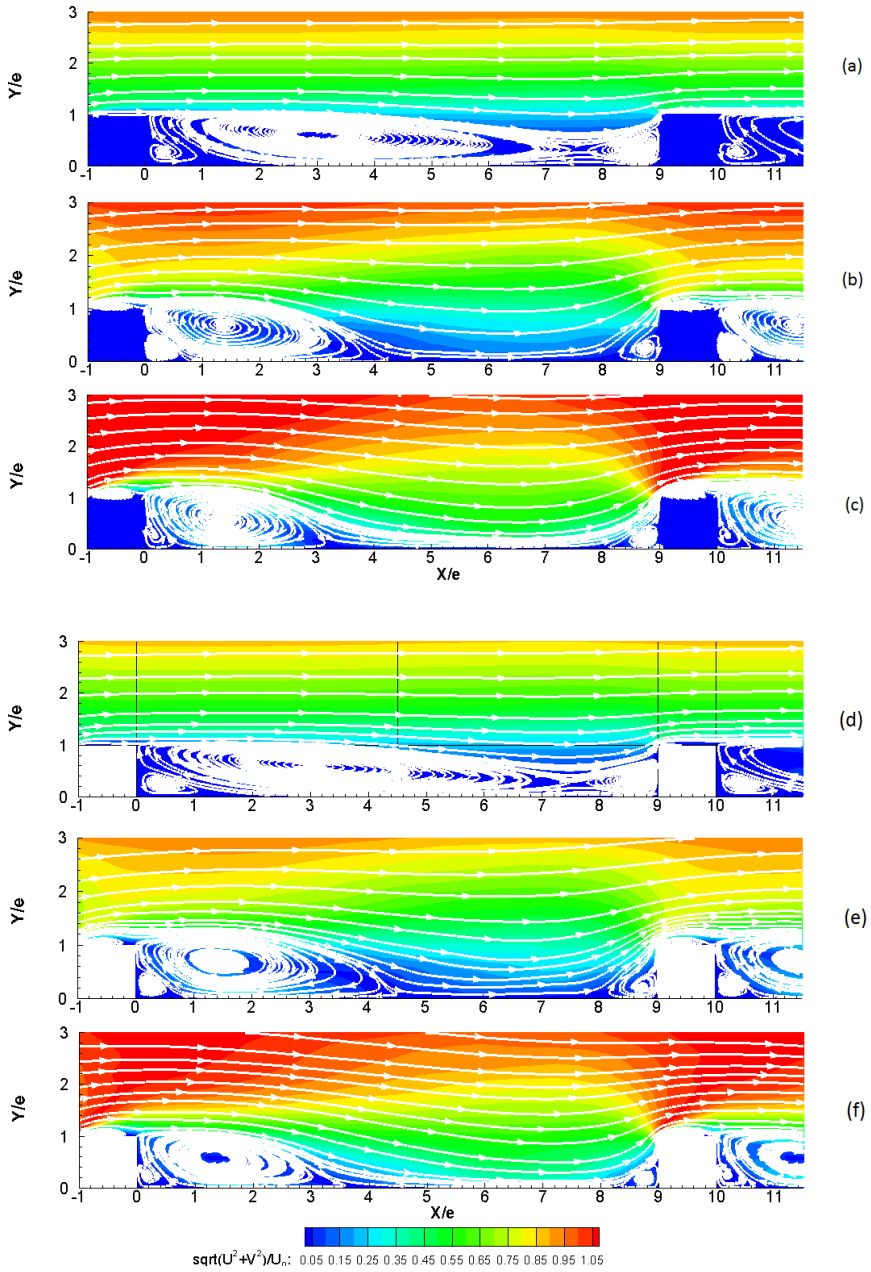

Figure 4.20: Time-averaged two-dimensional streamlines and contours of velocity magnitude distribution at center plane z=0.45: IBM stabilizing rotation (a); IBM stationary condition (b); IBM destabilizing rotation (c); BCG stabilizing rotation (d); BCG stationary c condition (e) and BCG destabilizing rotation (f).

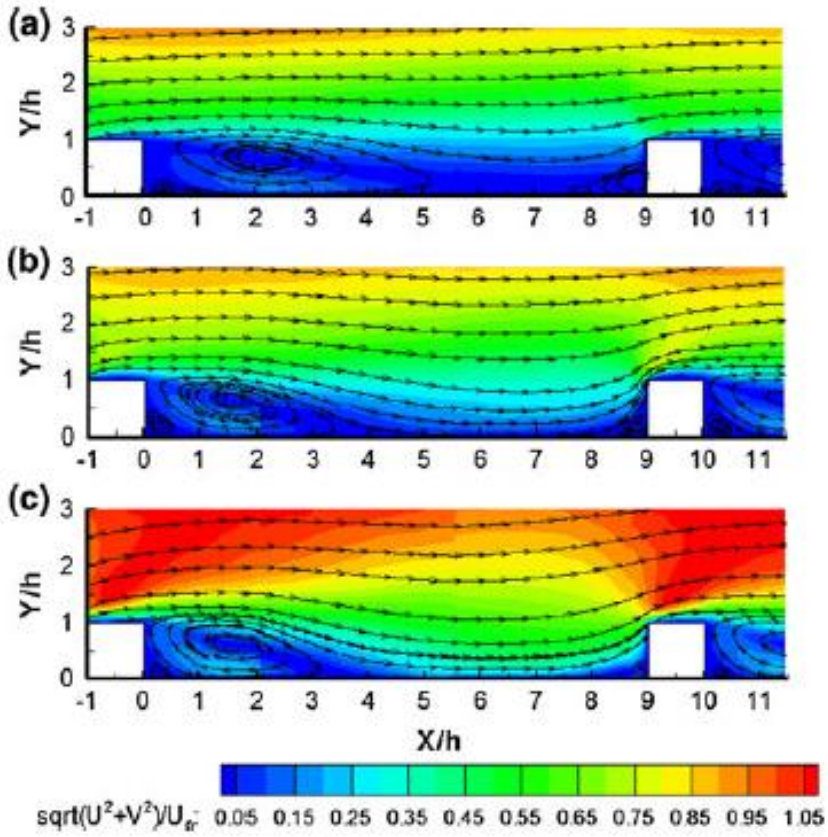

Figure 4.21: Two-dimensional streamlines and contours of mean in-plane velocity from experiment [16]**: stabilizing rotation (a), non-rotating case (b) and destabilizing rotation (c). (h is equivalent to the rib height e)**

Table 4.1: Reattachment length observed by IBM, BCG and experiment.

ROTATION NUMBER	IBM	BCG	EXPERIMENT
0 (STATIONARY)	4.2e	4.3e	3.85e
0.3 (DESTABILIZED)	3.5e	3.5e	3.45e
-0.3 (STABILIZED)	/	/	5.65e

4.2.2.2 Turbulence characteristics

Figure 4.22 shows the time-averaged turbulence statistics at center plane z=0.45. In the stationary duct, the maximum streamwise turbulence intensity (Urms) is observed at the upper leading edge of the rib in the separated shear layer at about 0.34. Under destabilizing rotation, turbulent intensity is much higher in this region, producing a much larger high Urms zone on top of the rib. On the other hand, in the stabilizing rotation, the maximum value is much smaller, and the high turbulence intensity zone on top of the rib does not exist. Comparing to the BCG method, IBM gives nearly the same results in stationary and stabilizing rotation. In the destabilizing rotation, the high streamwise turbulence intensity region on top of the rib from IBM prediction is much larger than it is in BCG prediction. Comparing to the experiment result, shown in Figure 4.23, both predictions from IBM and BCG agree very well with the experiment in stationary and stabilizing rotation case. In destabilizing rotation case, BCG has better agreement with the experiment than IBM.

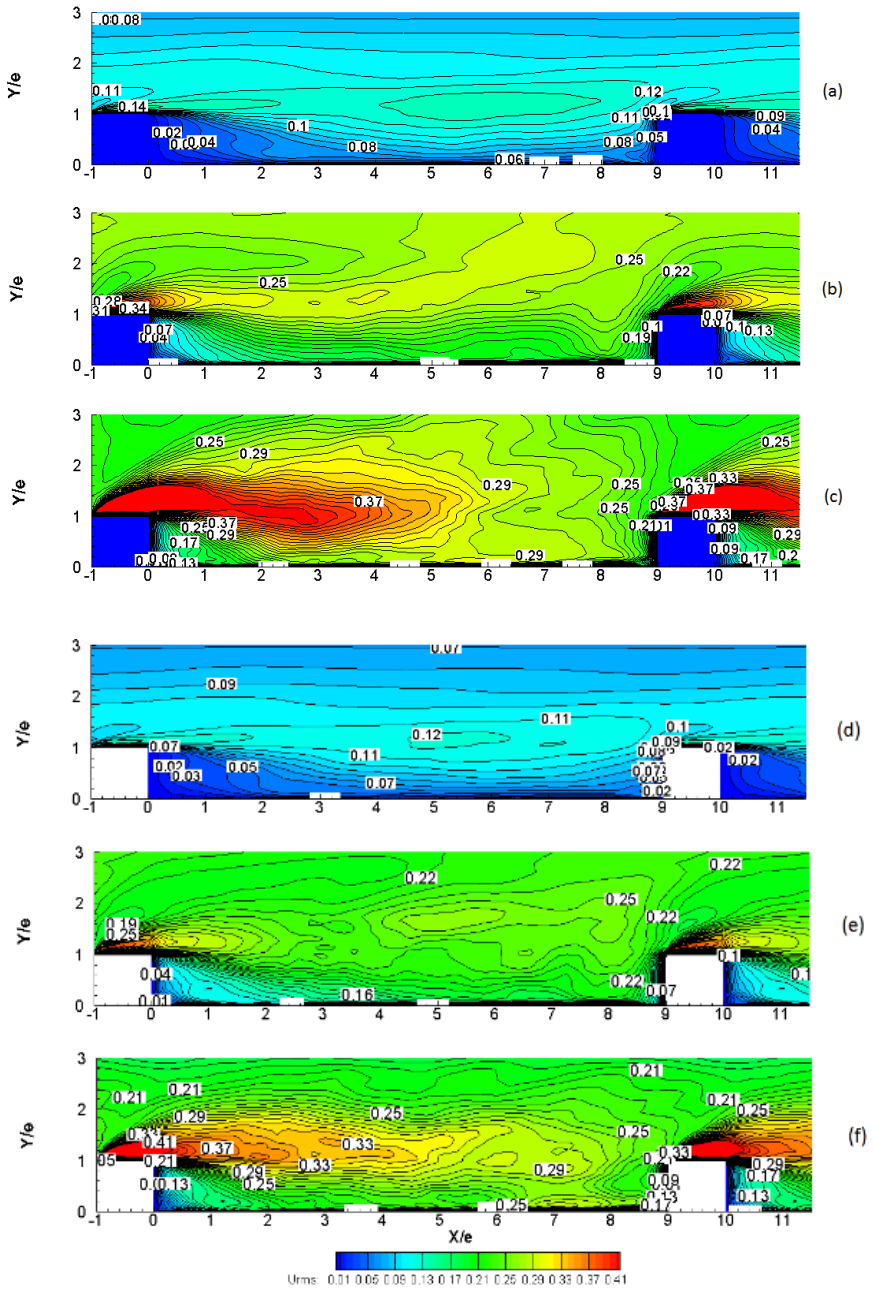

Figure 4.22: Time-averaged turbulence statistics Urms at center plane z=0.45: IBM stabilizing rotation (a); IBM stationary condition (b); IBM destabilizing rotation (c); BCG stabilizing rotation (d); BCG stationary condition (e) and BCG destabilizing rotation (f)

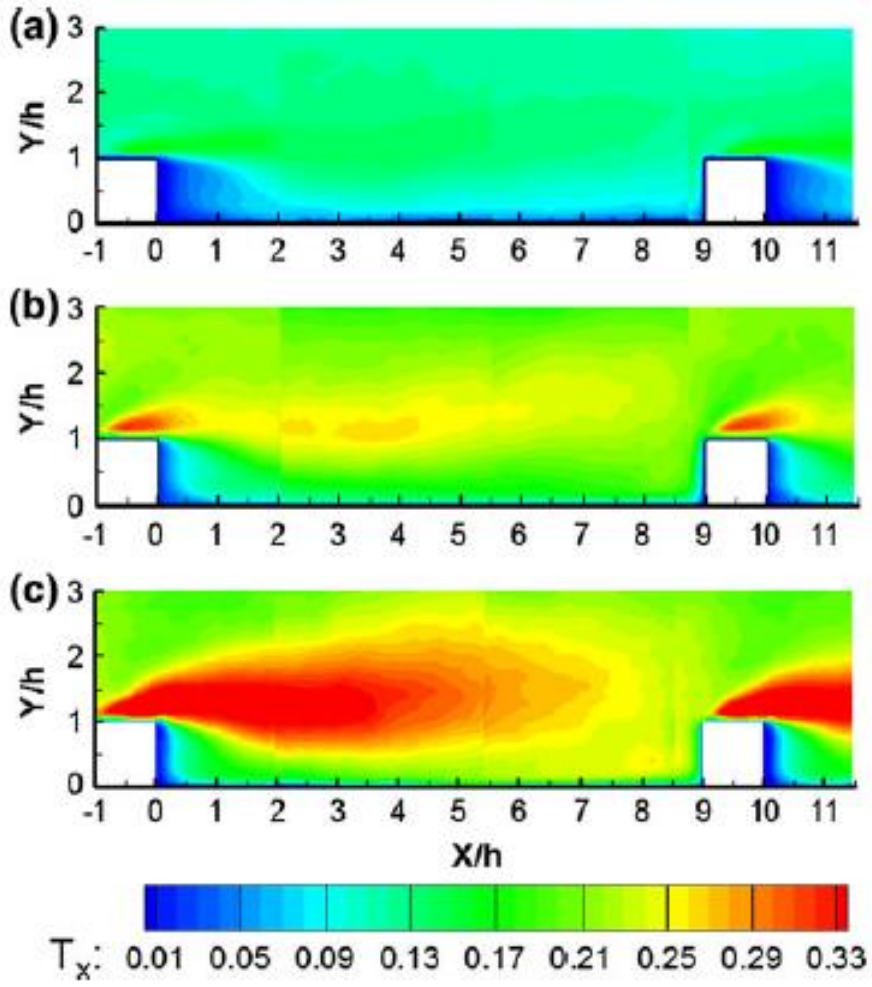

Figure 4.23: Contours of turbulence intensity along X-direction (Urms) from experiment [16]**: stabilizing rotation (a), non-rotating case (b), and destabilizing rotation (c). (h is equivalent to the rib height e)**

Vrms is presented in Figure 4.25. Because of the secondary flow induced by Coriolis forces, the high velocity flow from the center of the duct is pushed towards the rib wall in destabilizing rotation, resulting in a higher Y direction velocity near the rib wall region. This leads to higher Vrms values observed near the rib compared to the stationary case. In the stabilizing rotation, because the velocity magnitude is smaller (see Figure 3 (a) and (d)), the secondary flow created by the rib is also

weaker, the turbulent intensity is low, leaving a smaller Vrms region near the rib. Experiment results are shown in Figure 4.24. As with the Urms predcitons - IBM agrees well with BCG and experiment in stationary and stabilizing rotation, but slightly over predicts Vrms in destabilizing rotation.

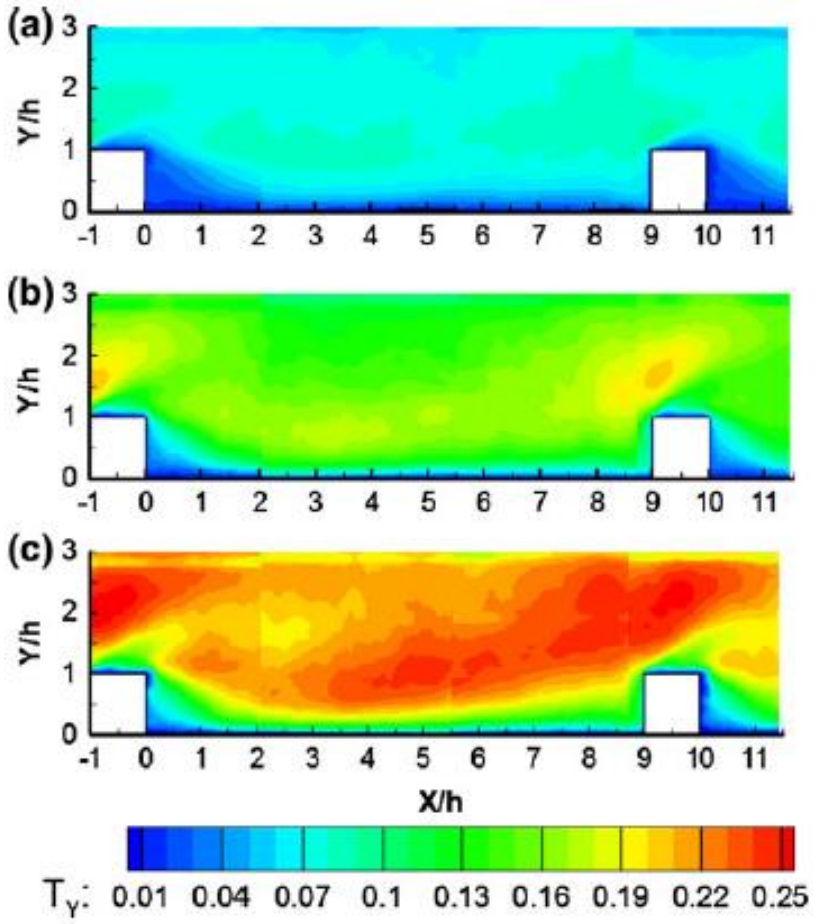

Figure 4.24: Contours of turbulence intensity along Y-direction (Vrms) from experiment [16]**: stabilizing rotation (a), non-rotating case (b), and destabilizing rotation (c). (h is equivalent to the rib height e)**

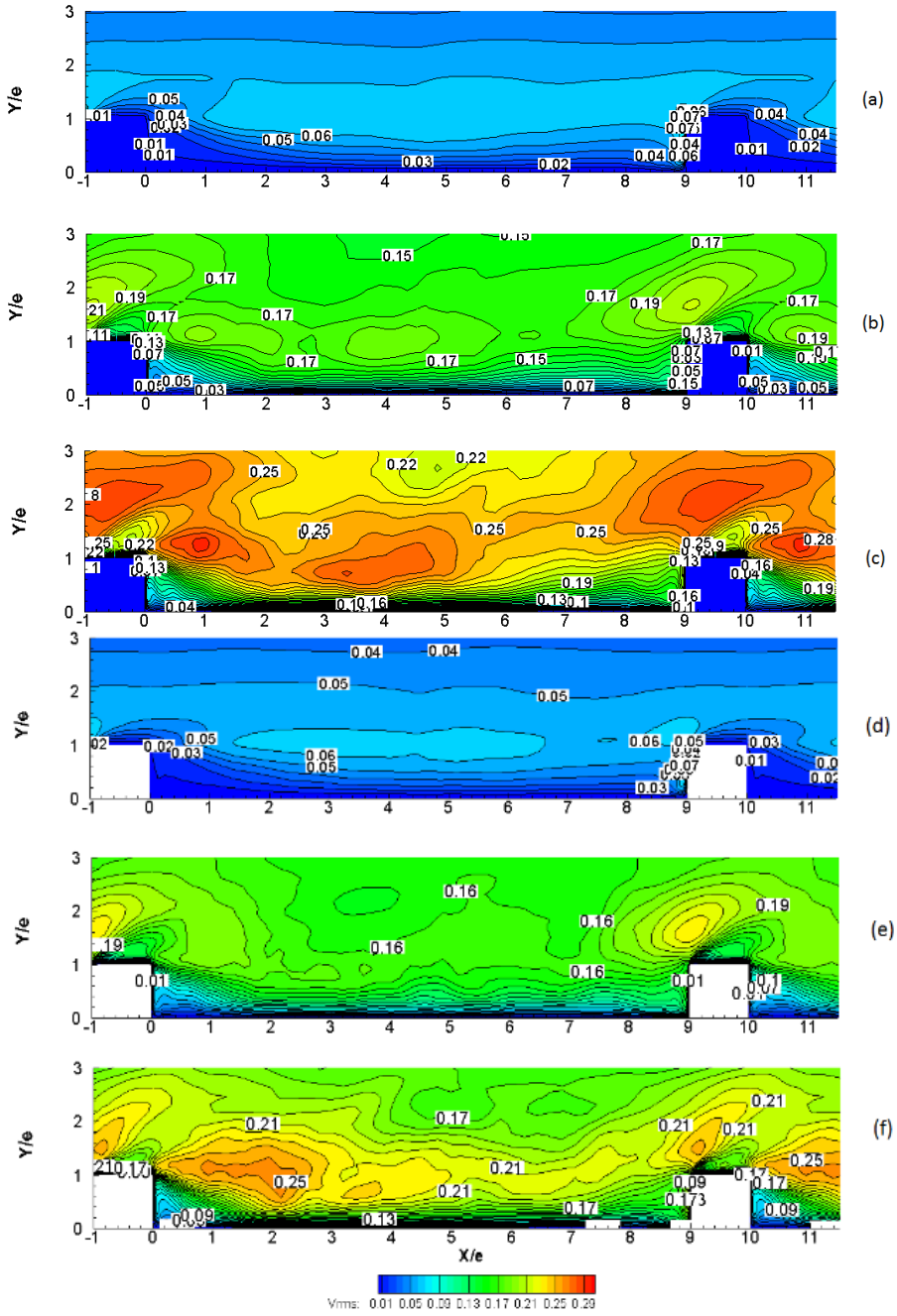

Figure 4.25: Time-averaged turbulence statistics Vrms at center plane z=0.45: IBM stabilizing rotation (a); IBM stationary condition (b); IBM destabilizing rotation (c); BCG stabilizing rotation (d); BCG stationary condition (e) and BCG destabilizing rotation (f)

Figure 4.26 presents the turbulent shear stress ($-\overline{u'v'}$) at center plane $z = 0.45$. In all the cases, the rib shear layer is the main source of the shear stress [16]. The difference between stationary case and stabilizing case is dramatic: a peak value of 0.025 is observed in stationary case which is 5 times the peak value of 0.004 in the stationary case. In destabilizing rotation, IBM predicts slightly higher shear stress than BCG. In stationary and stabilizing rotation case, IBM show good agreement with BCG. In the stabilizing rotation, IBM and BCG are both lower than the experiment results.

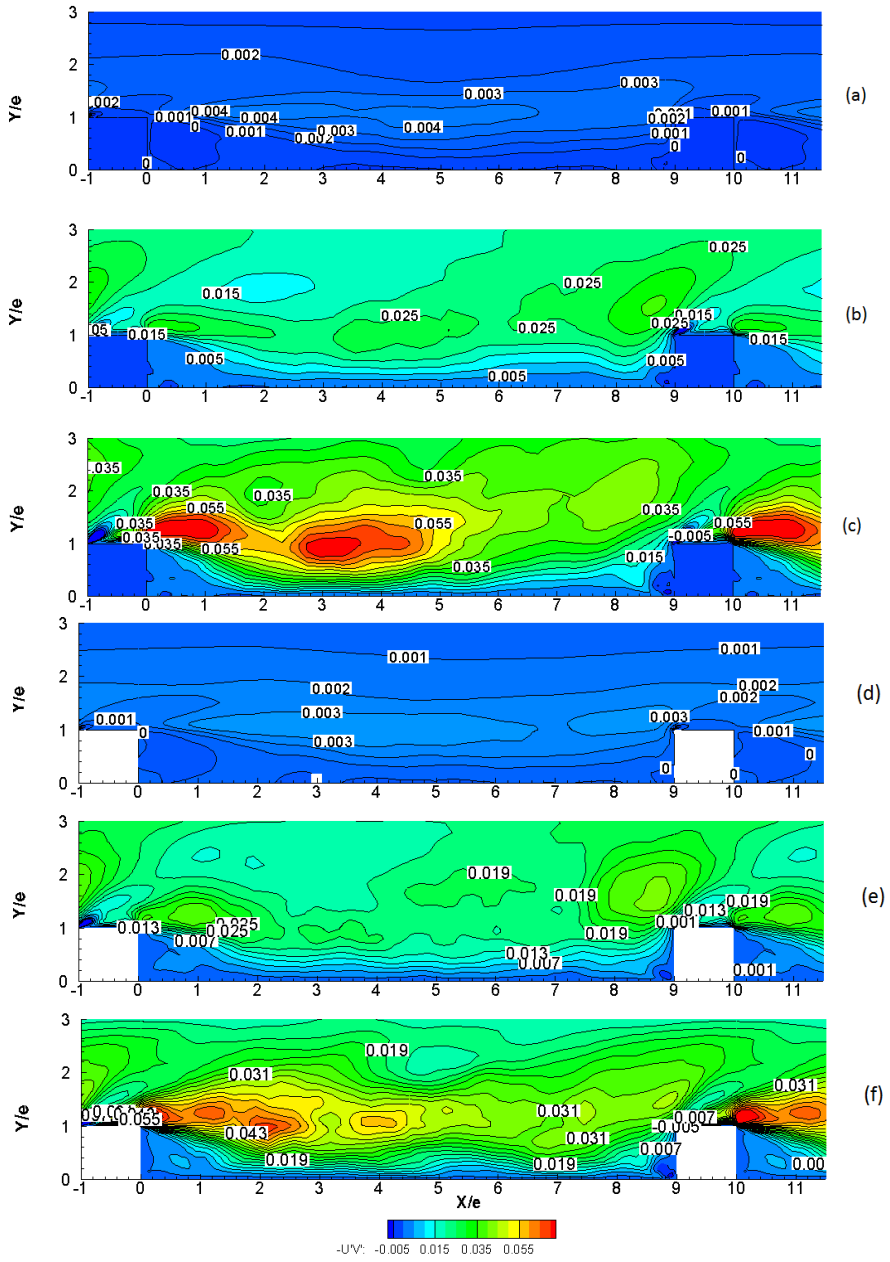

Figure 4.26: Time-averaged turbulent shear stress at center plane z=0.45: IBM stabilizing rotation (a); IBM stationary condition (b); IBM destabilizing rotation (c); BCG stabilizing rotation (d); BCG stationary condition (e) and BCG destabilizing rotation (f).

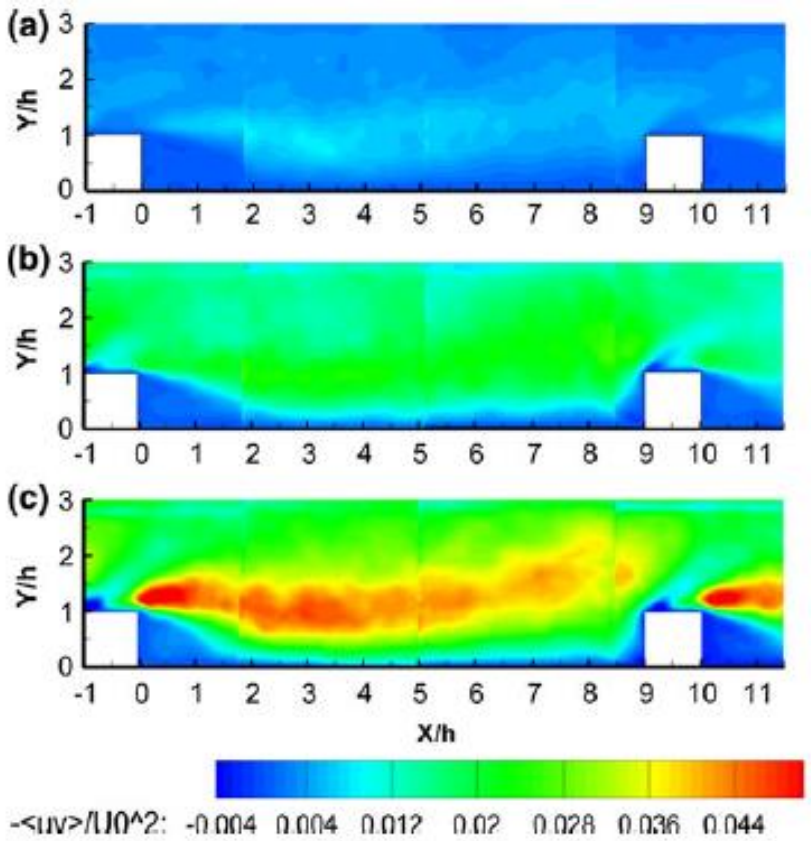

Figure 4.27: Contours of Reynolds shear stresses from experiment [16]**: stabilizing rotation (a), non-rotating case (b), and destabilizing rotation (c). (h is equivalent to the rib height e)**

4.2.2.3 Heat transfer

The local Nusselt number is calculated as:

$$Nu = \frac{1}{\theta_s - \theta_{ref}} \qquad \textbf{Equation 4.1}$$

Where θ_s is the surface temperature and θ_{ref} is the reference temperature defined as:

$$\theta_{ref} = \frac{\iint |u_1| \theta \, dA_x}{\iint |u_1| \, dA_x} \qquad \textbf{Equation 4.2}$$

The augmentation ratio is calculated based on the Dittus-Boelter correlation,

$$Nu_0 = 0.023 \cdot Re^{0.8} \cdot Pr^{0.4}. \qquad \textbf{Equation 4.3}$$

More details about the Nusselt number calculation can be found in Tafti [42].

Figure 4.28 to Figure 4.30 show the Nusselt number augmentation (Nu/Nu_0) distribution from IBM and BCG calculation for stationary case. On the smooth wall, higher heat transfer augmentation is observed in the vicinity of the rib junction, shown in Figure 4.28. This is because of the highly unsteady vortical structures induced by the rib-wall junction that impinge on the smooth wall making the flow highly 3D in this region. On the rib wall, shown in Figure 4.29, the peak augmentation is located at the upstream corner of the rib-wall junction where highly unsteady secondary junction eddies are produced. The region immediately after the rib, in the corner recirculation region, the augmentation is small due to low turbulence intensities. The augmentation increases in the primary recirculation region where the shed vortices from the rib reattach on the ribbed wall. Figure 4.30 shows the augmentation on the rib surfaces. On the upstream face (rib front), heat transfer coefficient reaches the maximum value at the leading edge as a result of high flow velocity. The augmentation is about 3 to 3.5 at the rib top due to the small recirculation zone formed by the separated shear layer. On the rib back, the augmentation is about 1 to 2.

Comparing to BCG results, the augmentation from IBM simulation is marginally smaller. In the primary recirculation zone, IBM predicts the augmentation about 2.2 to 2.5 which BCG gives 2.5 to 3. At the upstream corner of the rib-wall junction and at the rib top surface, IBM also under predicts the peak value about 20%.

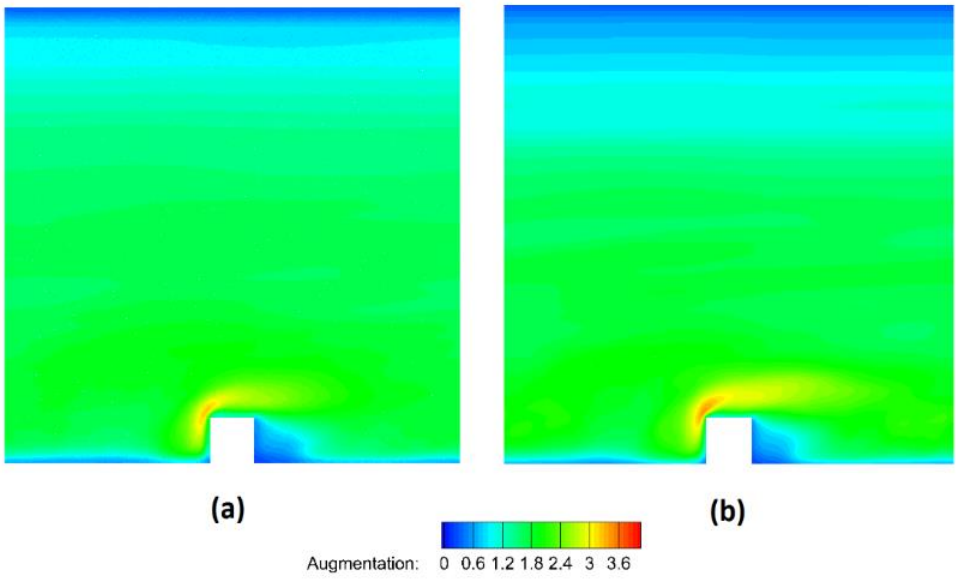

Figure 4.28: Contour of Nusselt number augmentation distribution on smooth wall: IBM (a); BCG (b).

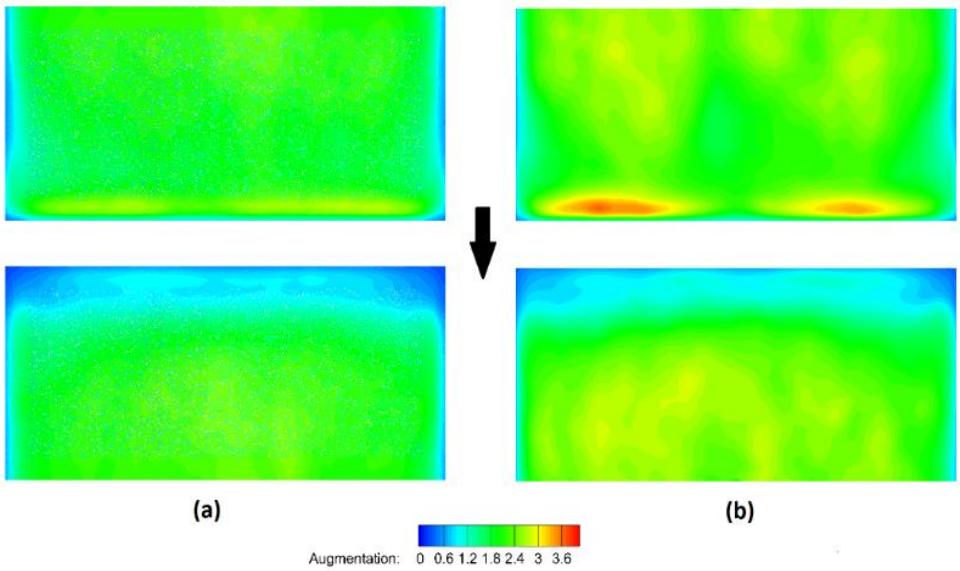

Figure 4.29: Contour of Nusselt number augmentation distribution on rib wall:IBM (a); BCG (b).

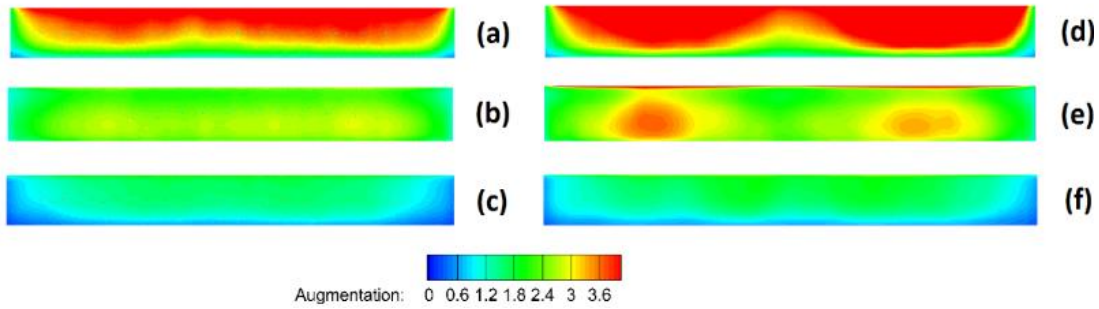

Figure 4.30: Contour of Nusselt number augmentation distribution on rib surface IBM upstream (a); IBM top (b); IBM downstream (c); BCG upstream (d); BCG top (e); BCG downstream (f).

4.2.2.4 Conclusion

The IBM simulation results of mean velocity fields and turbulence characteristics are compared with body conforming grid (BCG) predictions and PIV experimental data. These comparisons show that IBM can capture the flow characteristics accurately for a stationary ribbed duct. However, some discrepancies exist in the prediction of the size of the recirculation region for stabilized rotation with experiments. This trend is exhibited by both the body conforming grid and the IBM. Turbulent statistics predicted by IBM are also in good agreement with BCG calculations and experiments for stationary and stabilizing rotation. However, IBM over predicts turbulent normal and shear stresses in destabilizing rotation compared to BCG. Nusselt number augmentation results from IBM is compared with BCG results in the stationary case. Peak heat transfer coefficients are somewhat under predicted by the IBM.

Chapter 5

Wall Modeled LES in developing U-bend rib duct

As mentioned in chapter 4, although the Immersed Boundary Method can catch the geometry features without using a complex mesh, a fine grid is required near the immersed surface in order to properly resolve the boundary layer. The fineness of the grid is directly related to the Reynolds number of the flow, and the total amount of computational cells for the simulation increases proportionality to the amount of cells needed in the near wall region. For this reason, IBM has mostly been applied to low Reynolds number flows. To ease this grid requirement, Wall Modeled LES (WMLES) is introduced in this chapter. In wall modeled LES, the first layer of cells can locate at about $y^+ = 20 - 50$ instead of $y^+ = 1$ from the wall. This allows the near wall grid size to be much larger, and the simulation can use less computational cells than without the WMLES. For example, the first case presented in Chapter 4: IBM requires 2.3 million of cells for the background mesh while if Wall modeled LES is used, only 300 thousand cells, about 1/8 of the IBM case, will be required. The WMLES methodology has been briefly described in Chapter 2 and more details can be found in [34].

Because Wall Modeled LES with IBM algorithm is still under development, WMLES is tested with a body conforming grid in this chapter. WMLES is evaluated for simulating turbulent flow in a developing staggered ribbed U-bend duct. Three cases have been tested at a bulk Reynolds number of 10^5: a stationary case; a positive rotation case at a rotation number $R_o = 0.2$; and a negative rotation case at $R_o = -0.2$. Coriolis force effects are included in the calculation to evaluate the wall model under the influence of these effects which are known to affect shear layer turbulence

production on the leading and trailing sides of the duct. Wall model LES prediction is compared with experimental data [43].

5.1 Geometry and computational grid

The geometry, shown in Figure 5.1, consists of a square cross-sectioned two pass internal cooling duct with a 180° U-bend. Square-sectioned ribs are employed following a staggered arrangement along the inner and outer all. . A rib height to hydraulic diameter ratio, $e/D_h = 0.1$ and a rib pitch to rib height ratio, $p/e = 10$ is used for the rib geometry. Flow direction is shown by arrow: flow comes in from the inlet in the lower duct in negative x direction and leaves the outlet in the upper channel in positive x direction. Angular velocity is parallel to z-axis, and positive rotation direction is shown in Figure 5.1.

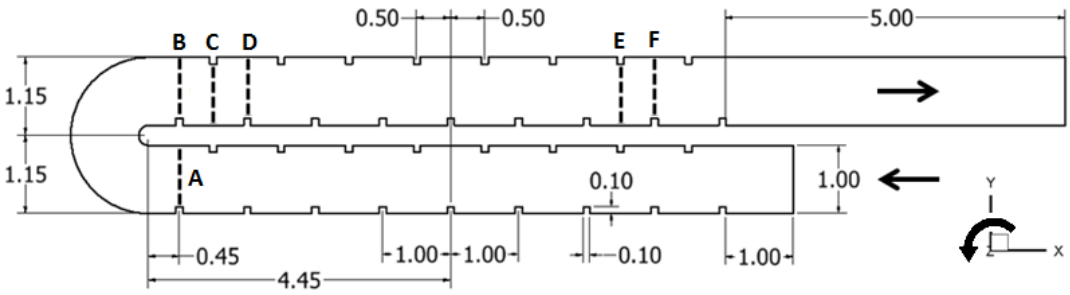

Figure 5.1: Computational domain and coordinate system.

The geometry are simulated on a body conforming grid with each rib pitch meshed with a 37,800 cells grid giving a total grid size of 7.78 million in the whole computational domain. The first layer of cells is spaced to give a y^+ approximately 20 at the walls. The dynamic Smagorinsky model is used together with a two-layer wall model (see Chapter 2 for details). The calculations are run for approximately 7 flow through time units with averaging performed over the last 5 units to obtain the mean and turbulent statistics.

5.2 Result and discussion

5.2.1 Stationary case

Figure 5.2 (a) shows the mean flow velocity vector at the center plane. Within the straight upstream duct section, the flow reaches fully developed states at the third rib pitch, with the same flow pattern being repeated at the second and the third inner rib. At the upstream entry of the bend, the effects of bend distort the velocity profile: flow accelerates near the inner side rib wall and separates as it traverses the tight inner radius. At the exit of the bend in the downstream duct, a big recirculation bubble is produced near the inner wall. The reattachment point is between the first and the second rib along the inner wall, leaving the first downstream rib inside this recirculation. Along the outer wall, flow accelerates because of the pressure gradient produced by the bend and reaches a high velocity before the first rib. The rib displaces the high momentum fluid toward the duct center, leaving a large recirculation zone behind the rib. The iso-surfaces of coherent vorticity which represents the turbulent intensity is shown in Figure 5.2 (b). Flow exit from the bend in the downstream is highly turbulent compare to the flow in the upstream duct. This turbulent intensity increment leads to higher heat transfer augmentation in the downstream duct.

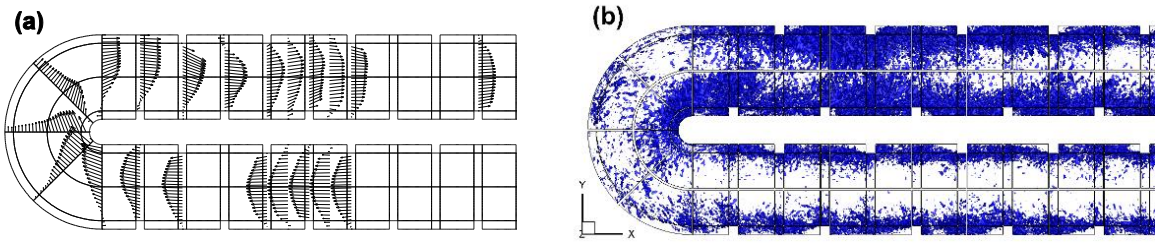

Figure 5.2: (a) Mean flow velocity vector at center plane (z=0.5);(b)coherent vorticity (level=17.5)

Figure 5.3 shows comparisons of mean velocity at select locations (see Figure 5.1) in the flow. The prediction captures the velocity distortion with very good accuracy at the entrance and the exit of the bend. Before entering the bend, flow shows a slightly high velocity on the inner side at location A while when coming out of the bend at location B, the outer side shows higher velocity, and a negative velocity is present on the inner side characterizing the separating zone. At location C and D, the velocity is still affected by the bend, leaving the peak velocity value near the outer wall.

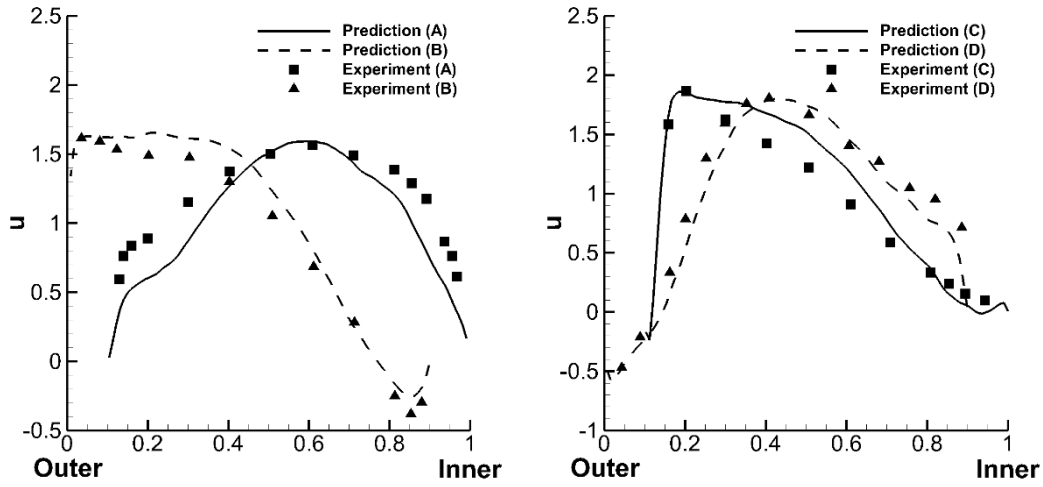

(a) (b)

Figure 5.3: Mean streamwise velocity at the center plane (z=0.5) : (a) at location A and B; (b) at location C and D. See Figure 5.1 for locations.

Figure 5.4 shows the turbulent statistic Urms comparisons between prediction and experimental data. The distributions of Urms are captured with very good accuracy by WMLES at all the locations except some disagreement of the peak value near the rib in the shear layer that forms on the rib.

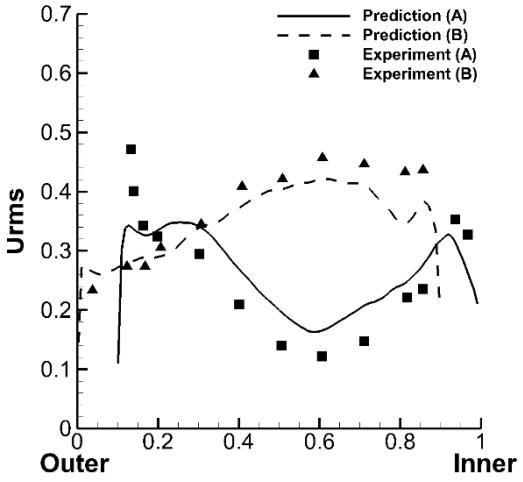

(a)

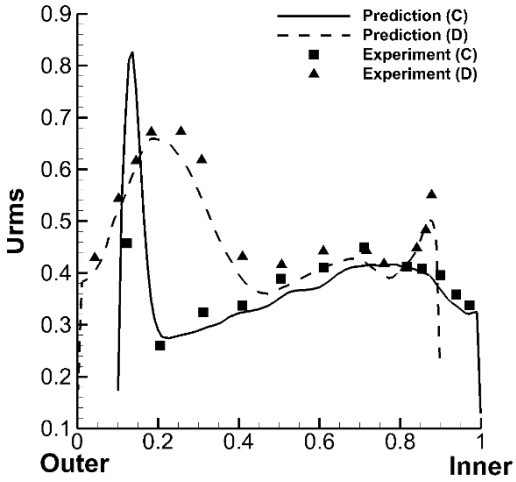

(b)

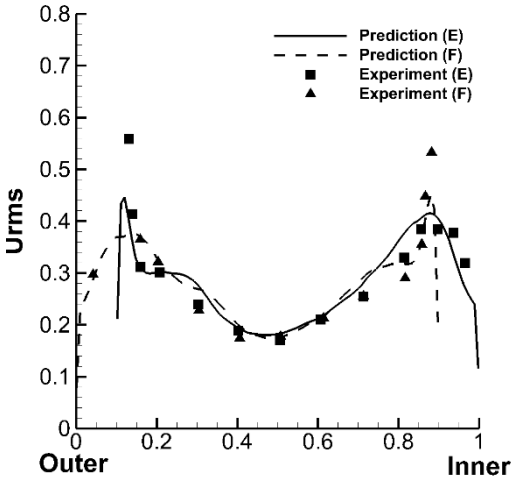

(c)

Figure 5.4: Turbulent statistics Urms : (a) at location A and B; (b) at location C and D; (c) at location E and F. See Figure 5.1 for locations.

Figure 5.5 show the turbulent shear stress in the downstream duct. The turbulent shear stress at the locations just coming out of the bend and fully developed rib pitch, also agree well with the

experiments. The low values of shear stress on the outside at location C are consistent with the small gradients in the predicted streamwise velocity seen at this location. At location E and F, the difference is very small which suggests that the flow is already restored to the fully developed state.

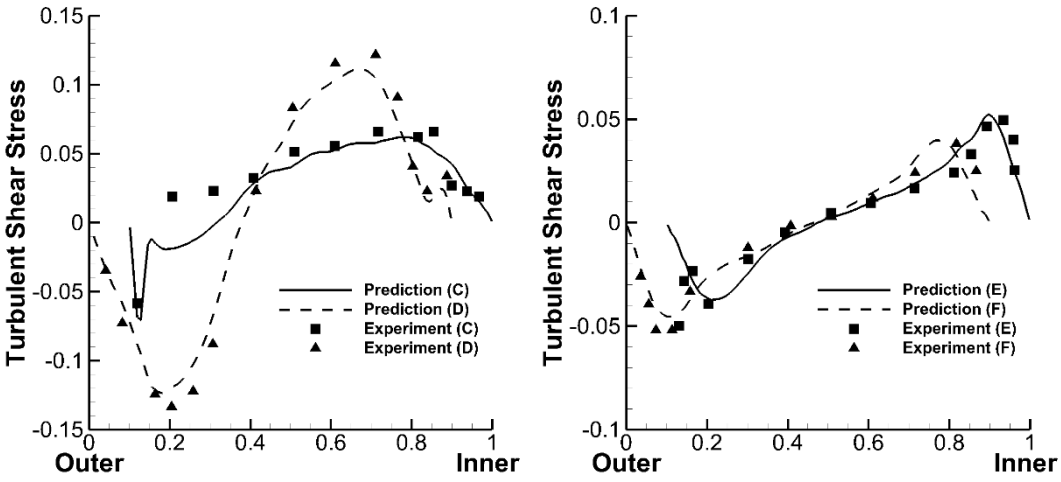

(a) (b)

Figure 5.5: Turbulent shear stress : (a) at location C and D; (b) at location E and F. See Fig. for locations.

5.2.2 Rotational Case

Figure 5.6.(a) and Figure 5.7 (a) shows the mean flow velocity vector at the center plane in positive rotation and negative rotation. In positive rotation, Coriolis forces push the flow toward the inner side of the duct, which acts as the leading wall in the upstream pass and trailing wall in the downstream pass. Comparing with stationary case, the inner bend separated shear layer creats a much larger recirculation zone in the downstream duct. The instantaneous coherent vorticity, in Figure 5.6 (b), clearly shows the augmentation and attenuation of turbulence at the inner and outer wall, respectively, in the first leg. Positive rotation also results in higher levels of turbulence than without

rotation at the exit of the bend. In negative rotation case, Coriolis forces have the opposite effects, pushing flow towards the outer wall. Because the mean flow is displaced by Coriolis force to the outer side, the flow velocity near the inner wall before the bend in negative rotation is smaller than in stationary and positive rotation case, producing a much smaller recirculation zone at the exit of the bend in the downstream duct. The instantaneous coherent vorticity in negative rotation, presented in Figure 5.7 (b), shows a turbulence augmentation and attenuation at the outer and inner wall. The turbulence near the outer wall in the bend and right after the bend is smaller than the positive rotation case.

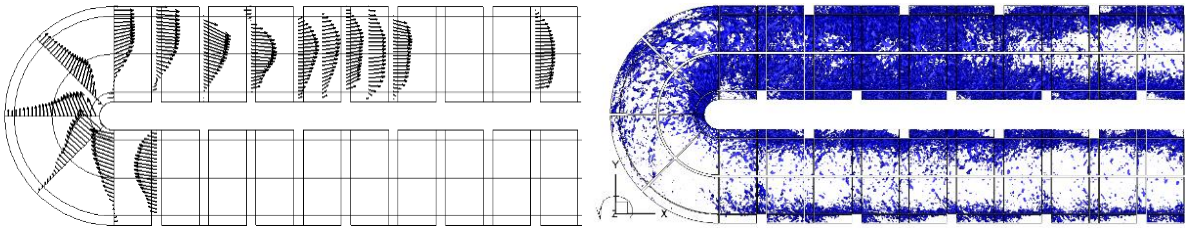

(a) (b)

Figure 5.6: Positive rotation Ro=0.2 : (a) Mean flow velocity vector at center plane (z=0.5);(b) coherent vorticity (level=17.5)

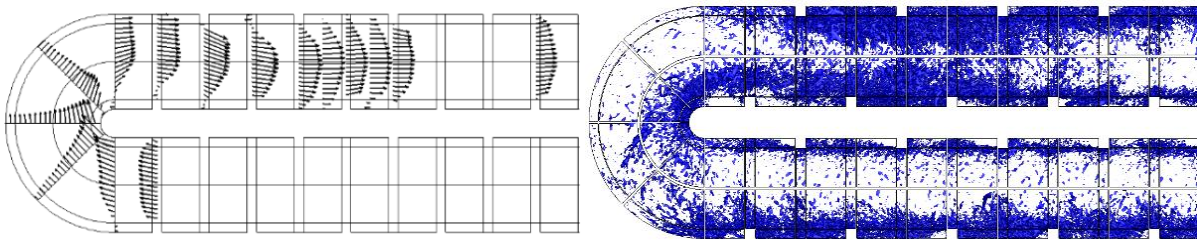

(a) (b)

Figure 5.7: Negative rotation Ro=-0.2 : (a) Mean flow velocity vector at center plane (z=0.5); (b) coherent vorticity (level=17.5)

Figure 5.8 shows the velocity comparison between prediction and experimental data at select locations. The predictions agree very well with the experiment. The Coriolis force effects on the velocity can be clearly seen in Figure 5.8 (a) and (b): at location A, positive rotation makes the flow accelerate near the inner wall, while negative rotation has higher velocity near the outer wall. Comparing to negative rotation, a higher pressure gradient need to be built in the bend to turn the flow in positive rotation case because of the higher velocity near the inner wall with a small turning radius. Velocity profile in location B shows that positive rotation has a larger negative velocity than negative rotation which agrees with velocity vector figure and instantaneous coherent vorticity figure: a larger recirculation zone is produced at the exit of the bend in positive rotation than negative rotation case. Figure 5.9 shows the turbulent statistics U_{rms} in positive rotation and negative rotation. In general the predictions agree very well with the experimental data. There is some difference between prediction and experiment in negative rotation case at the locations before the U-bend (location A) and right after the bend (location B and C). WMLES over predicts the turbulent shear stress, shown in Figure 5.10 (a), at location C and D in positive rotation, but this over prediction is very small. In general, all the comparisons between WMLES prediction and experimental data show that WMLES catches the flow features with reasonable accuracy, considering the complexity of the turbulent interactions.

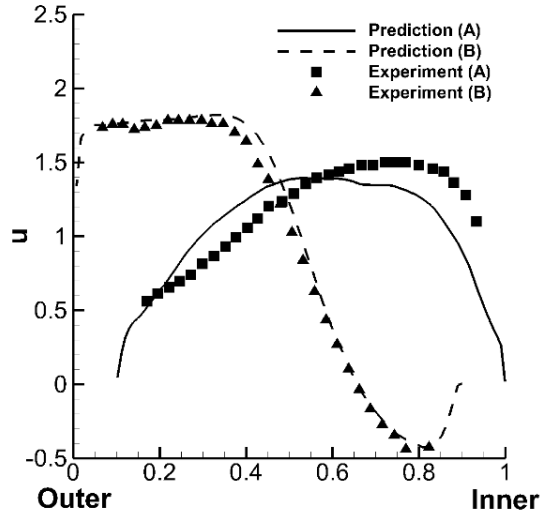

(a)

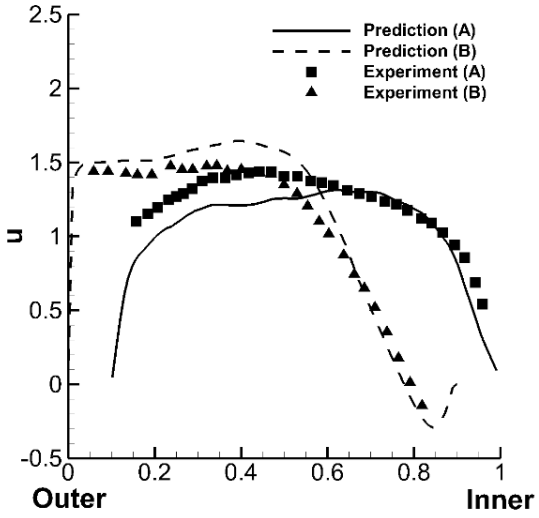

(b)

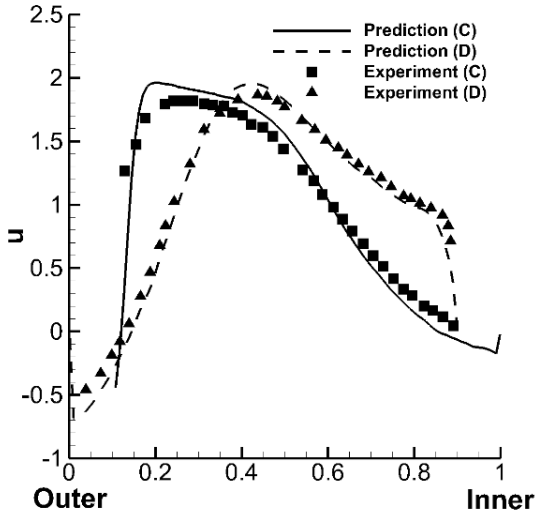

(a)

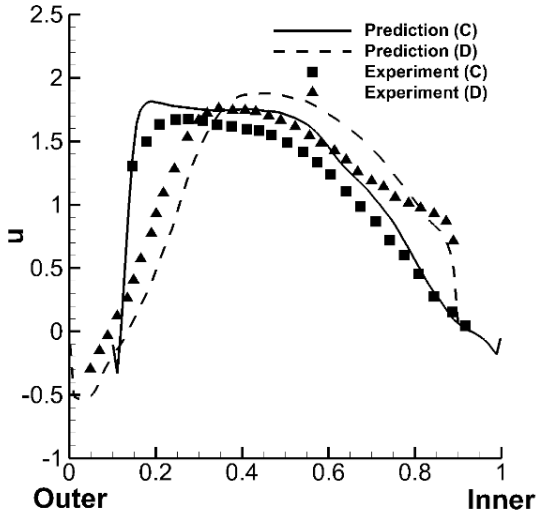

(b)

Figure 5.8: Mean streamwise velocity at the center plane (z=0.5):Positive rotation (a) and (c); Negative rotation (b) and (d). See Figure 5.1 for locations.

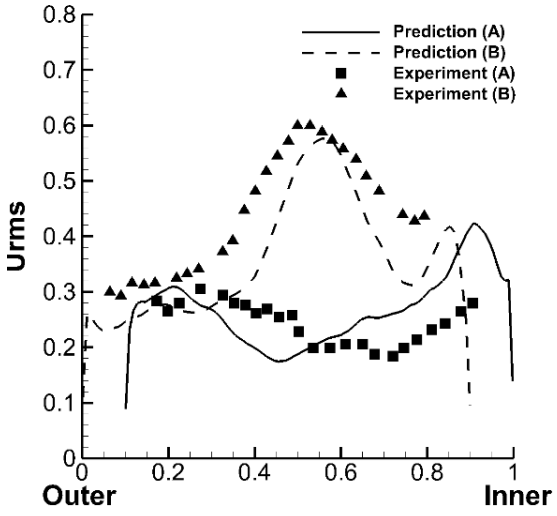
Prediction (A)
Prediction (B)
Experiment (A)
Experiment (B)
Urms
Outer
Inner

(a)

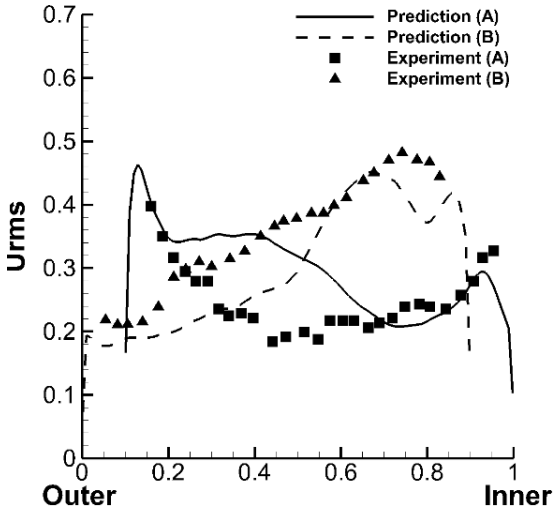
Prediction (A)
Prediction (B)
Experiment (A)
Experiment (B)
Urms
Outer
Inner

(b)

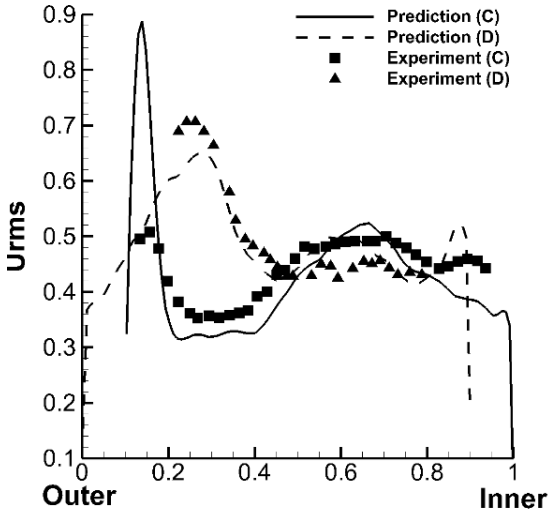
Prediction (C)
Prediction (D)
Experiment (C)
Experiment (D)
Urms
Outer
Inner

(c)

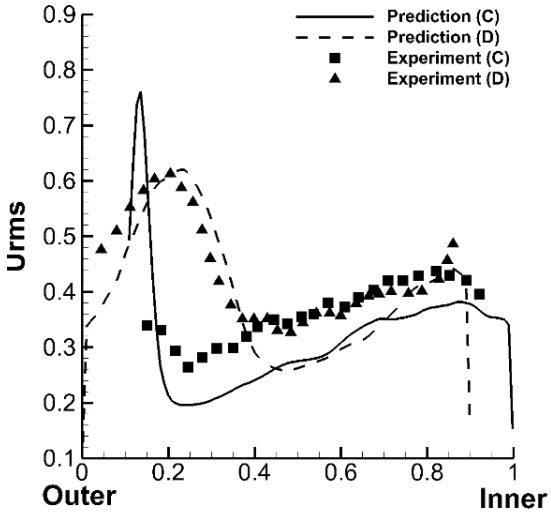
Prediction (C)
Prediction (D)
Experiment (C)
Experiment (D)
Urms
Outer
Inner

(d)

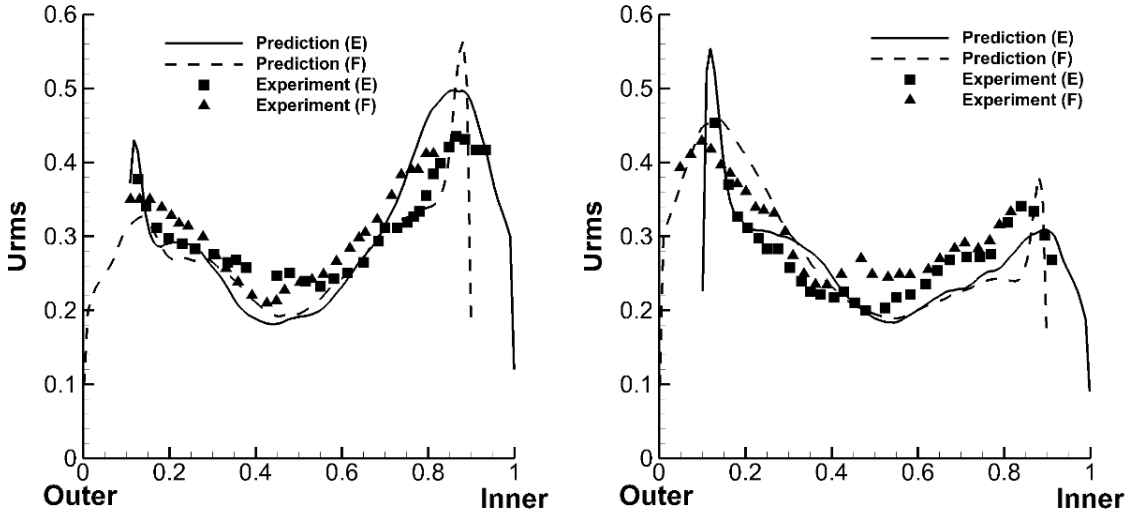

(e) (f)

Figure 5.9: Turbulent statistics Urms: Positive rotation (a),(c) and (e); Negative rotation (b), (d) and (f). See Figure 5.1 for locations.

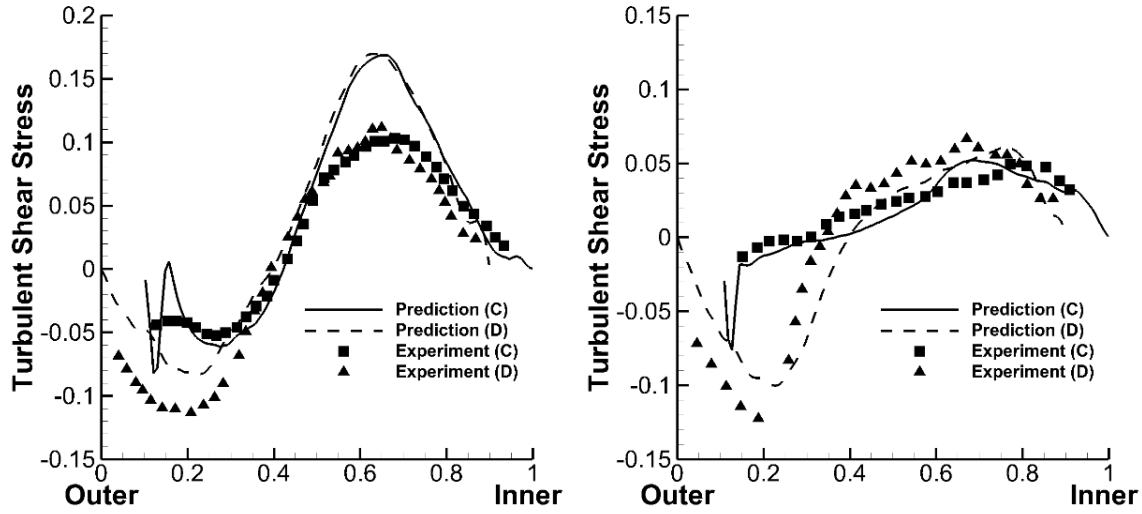

(a) (b)

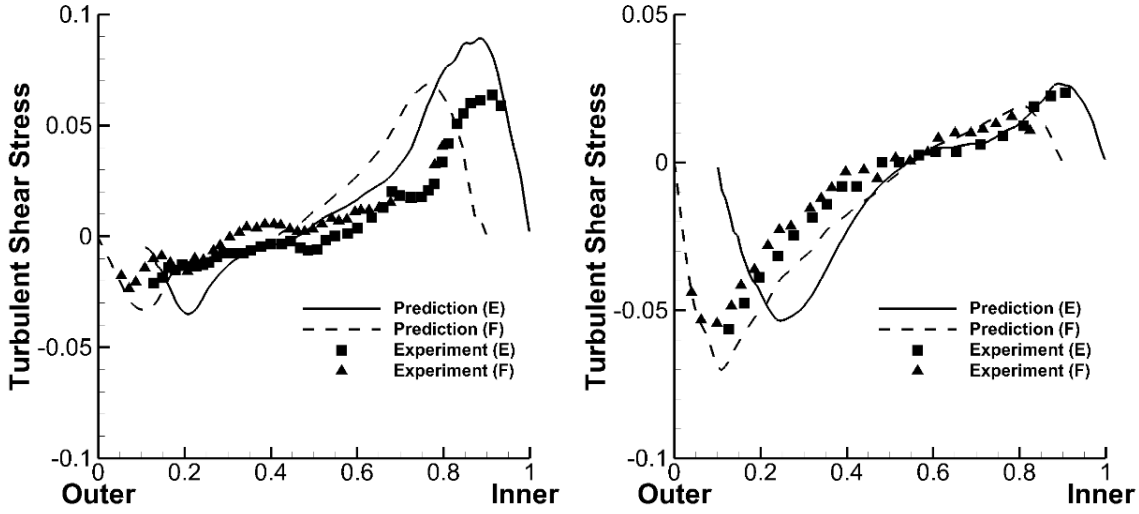

(c) (d)

Figure 5.10: Turbulent shear stress: Positive rotation (a) and (c); Negative rotation (b) and (d).

See Figure 5.1 for locations.

Chapter 6

Summary and Conclusion

In this thesis, a frame work based on Immersed Boundary Method (IBM) is evaluated to resolve the intricate geometrical features in the simulation model. In this frame work, complex geometry surface is immersed into a volume background grid. The immersed surface cuts through the background mesh and proper boundary conditions are formulated for the fluid domain. Since the surface is not resolved exactly as in a body conformed grid, very fine mesh is required in the vicinity of the immersed boundary to get resolve the geometry accurately. The fineness of the grid is directly related to the Reynolds number of the flow, and the total number of computational cells for the simulation increases in proportionality to the number of cells needed in the near wall region. For this reason, IBM has mostly been applied to low Reynolds number flows. To ease this grid requirement, Wall Modeled LES (WMLES) is also introduced in this thesis. In wall modeled LES, the first layer of cells can be located at about $y^+ = 20 - 50$ instead of $y^+ = 1$ from the wall. This allows the near wall grid size to be much larger, and the simulation can use less computational cells than without the WMLES.

In Chapter 3, immersed boundary method frame work is tested for turbulent flow. DNS simulation is performed for two benchmark test cases: fully developed channel flow and pipe flow.IBM simulation data are compared with well-accepted DNS results for channel flow and with LDV measurements in pipe flow. These comparisons show that IBM can capture the flow characteristics as accurately as the traditional body conforming grid methods.

In Chapter 4, IBM is further investigated in ribbed duct geometry used in internal cooling passages of gas turbine blades. Two geometries are tested: Case 1, an orthogonal non-staggered

ribbed duct is simulated at $Re = 20{,}000$. Velocity field, turbulent statistics and Nusselt number from IBM predictions are compared with body conforming grid simulation results [42]; Case 2, a one side ribbed duct is simulated at $Re = 15{,}000$ and under 3 rotation numbers: $Ro = 0.3$, $Ro = -0.3$ and $Ro = 0.0$ (stationary). For these cases, the simulation results are compared with PIV experiment data [16]. The dynamic Smagorinsky subgird stress model is used with a second-order central difference discretization for these two cases. In both cases, IBM captures the flow characteristics with good accuracy. In heat transfer cases, the nusselt number augmentation distribution predictions from IBM agree well with the BCG results. However, the peak heat transfer coefficients are somewhat under predicted by the IBM.

In Chapter 5, wall modeled LES is tested with a body conforming grid in this chapter. WMLES is evaluated for simulating turbulent flow in a developing staggered ribbed U-bend duct. Three cases have been tested at a bulk Reynolds number of 10^5: a stationary case; a positive rotation case at a rotation number $Ro = 0.2$; and a negative rotation case at $Ro = -0.2$. Coriolis force effects are included in the calculation to evaluate the wall model under the influence of these effects which are known to affect shear layer turbulence production on the leading and trailing sides of the duct. WMLES results show very good agreement with the experiment.

In summary, the overall good agreement between IBM, BCG and experimental results suggest that IBM is a promising method to apply to complex blade geometries. However, without the wall modeled LES, IBM applications will be limited to a relatively low Reynolds number due to the grid requirement near the immersed surface. Future work will focus on increase the predicting accuracy of the heat transfer coefficients and combining the IBM with WMLES.

Bibliography

[1] Han, J.-C., 2013, "Fundamental Gas Turbine Heat Transfer," Journal of Thermal Science and Engineering Applications, **5**(2), p. 021007.

[2] Han, J.-C., Dutta, S., and Ekkad, S., 2012, Gas Turbine Heat Transfer and Cooling Technology, CRC Press.

[3] Tafti, D. K., He, L., and Nagendra, K., 2014, "Large eddy simulation for predicting turbulent heat transfer in gas turbines Large eddy simulation for predicting turbulent heat transfer in gas turbines," Philosophical Transactions of The Royal Society A, **372**(July).

[4] Han, J., 1984, "Heat transfer and friction in channels with two opposite rib-roughened walls," Journal of heat transfer, **106**(November 1984).

[5] Han, J., 1988, "Heat transfer and friction characteristics in rectangular channels with rib turbulators," Journal of Heat transfer, **110**(May 1988).

[6] Al-Qahtani, M., Chen, H., and Han, J., 2002, "A numerical study of flow and heat transfer in rotating rectangular channels (AR= 4) with 45 rib turbulators by Reynolds stress turbulence model," Proceedings of ASME EXPO 2002.

[7] Ekkad, S. V., and Han, J.-C., 1997, "Detailed heat transfer distributions in two-pass square channels with rib turbulators," International Journal of Heat and Mass Transfer, **40**(11), pp. 2525–2537.

[8] Chandra, P., Han, J., and Lau, S., 1988, "Effect of rib angle on local heat/mass transfer distribution in a two-pass rib-roughened channel," Journal of Turbomachinery, **110**.

[9] Han, J., and Zhang, P., 1991, "Effect of rib-angle orientation on local mass transfer distribution in a three-pass rib-roughened channel," Journal of Turbomachinery, **113**(January 1991).

[10] Zhang, Y., and Han, J., 1995, "Surface heating effect on local heat transfer in a rotating two-pass square channel with 60 deg angled rib turbulators," Journal of Turbomachinery, **117**(April 1995), pp. 272–280.

[11] Wagner, J., 1991, "Heat transfer in rotating serpentine passages with smooth walls," Journal of Turbomachinery, **113**(July 1991), pp. 321–330.

[12] Liou, T., and Chen, C., 1999, "LDV study of developing flows through a smooth duct with a 180 deg straight-corner turn," Journal of turbomachinery, **121**(January 1999), pp. 167–174.

[13] Liou, T.-M., Chen, M.-Y., and Tsai, M.-H., 2002, "Fluid Flow and Heat Transfer in a Rotating Two-Pass Square Duct With In-Line 90-deg Ribs," Journal of Turbomachinery, **124**(2), p. 260.

[14] Taslim, M., Rahman, A., and Spring, S. D., 1991, "An experimental investigation of heat transfer coefficients in a spanwise rotating channel with two opposite rib-roughened walls," Journal of Turbomachinery, **113**(January 1991), pp. 75–82.

[15] Wagner, J., 1992, "Heat transfer in rotating serpentine passages with trips normal to the flow," Journal of Turbomachinery, **114**(October 1992).

[16] Coletti, F., Maurer, T., Arts, T., and Di Sante, A., 2011, "Flow field investigation in rotating rib-roughened channel by means of particle image velocimetry," Experiments in Fluids, **52**(4), pp. 1043–1061.

[17] Iaccarino, G., Ooi, A., Reif, B., and Durbin, P., 1999, RANS simulations of rotating flows.

[18] Liou, T.-M., Hwang, J.-J., and Chen, S.-H., 1993, "Simulation and measurement of enhanced turbulent heat transfer in a channel with periodic ribs on one principal wall," International Journal of Heat and Mass Transfer, **36**(2), pp. 507–517.

[19] Jia, R., Saidi, A., and Sundén, B., 2002, "Heat transfer enhancement in square ducts with V-shaped ribs of various angles," ASME TURBO EXPO 2002, pp. 1–8.

[20] Iacovides, H., and Launder, B., 1991, "Parametric and numerical study of fully developed flow and heat transfer in rotating rectangular ducts," Journal of Turbomachinery, **113**(90).

[21] Bo, T., Iacovides, H., and Launder, B., 1995, "Developing buoyancy-modified turbulent flow in ducts rotating in orthogonal mode," Journal of Turbomachinery, **117**(July 1995).

[22] Yang, K.-S., and . Ferzigert, J. H., 1993, "Large-Eddy Simulation of Turbulent Obstacle Flow Using a Dynamic Subgrid-Scale Model," AIAA Journal, **31**(8), pp. 1406–1413.

[23] Murata, A., and Mochizuki, S., 2004, "Large eddy simulation of turbulent heat transfer in a rotating two-pass smooth square channel with sharp 180° turns," International Journal of Heat and Mass Transfer, **47**(4), pp. 683–698.

[24] Tyagi, M., and Acharya, S., 2005, "Large Eddy Simulations of Flow and Heat Transfer in Rotating Ribbed Duct Flows," Journal of Heat Transfer, **127**(5), p. 486.

[25] Ahn, J., Choi, H., and Lee, J. S., 2005, "Large Eddy Simulation of Flow and Heat Transfer in a Channel Roughened by Square or Semicircle Ribs," Journal of Turbomachinery, **127**(2), p. 263.

[26] Viswanathan, A. K., and Tafti, D. K., 2007, "Investigation of Detached Eddy Simulations in Capturing the Effects of Coriolis Forces and Centrifugal Buoyancy in Ribbed Ducts," Journal of Heat Transfer, **129**(7), p. 778.

[27] Viswanathan, A. K., and Tafti, D. K., 2005, "Detached Eddy Simulation of Turbulent Flow and Heat Transfer in a Ribbed Duct," Journal of Fluids Engineering, **127**(5), p. 888.

[28] Watanabe, K., and Takahashi, T., 2002, "LES simulation and experimental measurement of fully developed ribbed channel flow and heat transfer," Proceedings of ASME TURBO EXPO 2002.

[29] Saha, A. K., and Acharya, S., 2003, "Flow and Heat Transfer in an Internally Ribbed Duct with Rotation: an Assessment of LES and URANS," Proceedings of ASME Turbo Expo 2003.

[30] Abdel-Wahab, S., and Tafti, D. K., 2004, "Large Eddy Simulation of Flow and Heat Transfer in a 90 deg Ribbed Duct With Rotation: Effect of Coriolis and Centrifugal Buoyancy Forces," Journal of Turbomachinery, **126**(4), p. 627.

[31] Tafti, D. K., 2001, "GenIDLEST - A scalable parallel computational tool for simulating complex turbulent flows," Proceedings of the ASME Fluids Engineering Division (FED), ASME-IMECE, p. Vol.256.

[32] Tafti, D. K., 2011, "Time-accurate techniques for turbulent heat transfer analysis in complex geometries, Advances in Computational Fluid Dynamics and Heat Transfer," Developments in Heat Transfer, R. Amano, and B. Sunden, eds., WIT PRESS.

[33] Nagendra, K., Tafti, D. K., and Viswanath, K., 2014, "A new approach for conjugate heat transfer problems using immersed boundary method for curvilinear grid based solvers," Journal of Computational Physics, **267**, pp. 225–246.

[34] Patil, S., and Tafti, D., 2012, "Two-Layer Wall Model for Large-Eddy Simulations of Flow over Rough Surfaces," AIAA Journal, **50**(2), pp. 454–460.

[35] Patankar, S., 1977, "Fully developed flow and heat transfer in ducts having streamwise-periodic variations of cross-sectional area," Transactions of the ASME, **99**(May 1977), pp. 180–186.

[36] Zhang, L., and Tafti, D., 1997, "Computations of flow and heat transfer in parallel-plate fin heat exchangers on the CM-5: effects of flow unsteadiness and three-dimensionality," International Journal of Heat and mass transfer, **40**(6).

[37] Gilmanov, A., and Sotiropoulos, F., 2005, "A hybrid Cartesian/immersed boundary method for simulating flows with 3D, geometrically complex, moving bodies," Journal of Computational Physics, **207**(2), pp. 457–492.

[38] Chapman, D. R., 1979, “Computational Aerodynamics Development and Outlook,” AIAA Journal, **17**(12), pp. 1293–1313.

[39] January, G. R., Reynolds, H., Stokes, N.-, and Sgs, T., 1975, “Subgrid Scale Model for Finite Difference Simulations of Turbulent Flows in Plane Channels and Annuli,” Journal of Computational Physics, **404**, pp. 376–404.

[40] Kim, J., Moin, P., and Moser, R., 1987, “Turbulence statistics in fully developed channel flow at low Reynolds number,” Journal of Fluid Mechanics, **177**, pp. 133–166.

[41] Den Toonder, J. M. J., and Nieuwstadt, F. T. M., 1997, “Reynolds number effects in a turbulent pipe flow for low to moderate Re,” Physics of Fluids, **9**(11), p. 3398.

[42] Tafti, D. K., 2005, “Evaluating the role of subgrid stress modeling in a ribbed duct for the internal cooling of turbine blades,” International Journal of Heat and Fluid Flow, **26**(1), pp. 92–104.

[43] Iacovides, H., and Jackson, D., 1998, “LDA study of the flow development through an orthogonally rotating U-bend of strong curvature and rib-roughened walls,” Journal of Turbomachinery, **120**(April 1998).